Title
Direct Observation of Colloidal Nanocrystals by Using Liquid Cell Transmission Electron Microscopy

Author
Park, Jungwon

Publication Date
2012

Peer reviewed|Thesis/dissertation

Direct Observation of Colloidal Nanocrystals by Using Liquid Cell Transmission Electron Microscopy

By

Jungwon Park

A dissertation is submitted in partial satisfaction of the

requirements for the degree of

Doctor of Philosophy

in

Chemistry

in the

Graduate Division

of the

University of California, Berkeley

Committee in charge:

Professor A. Paul Alivisatos, Chair
Professor Gabor A. Somorjai
Professor Junqiao Wu

Spring 2012

Abstract

Direct Observation of Colloidal Nanocrystals by

Using Liquid Cell Transmission Electron Microscopy

by

Jungwon Park

Doctor of Philosophy in Chemistry

University of California, Berkeley

Professor A. Paul Alivisatos, Chair

Colloidal semiconductor and metal nanocyrstals receive attention from studying their physical properties to application in biology, electronics, optics, and catalyst. In addition, colloidal nanocrystals as artificial building blocks construct assemblies in solution phase and on substrate to exploit coupled properties of individual nanocrystals. A facile control of physical properties by tuning size, shape, and composition of nanocrystals can be achieved in solution phase synthetic protocols and now we have a library of literatures about them.

However, most of nanocrystal synthesis and their use are developed empirically, perhaps in a lack of fundamental understanding. Growth kinetics during synthesis, motion and behavior of nanocrystals in liquid and at interfaces include many questions which await mechanistic studies.

This dissertation explores direct observation of nanocrystals in liquid by using liquid cell transmission electron microscopy. Growth of nanocrystals from molecular precursor in solvent requires observation in atomistic resolution of a single particle level. Chapter 1 describes single particle growth trajectories of metal nanocrystals investigated by using graphene liquid cell in transmission electron microscopy. This cell is employed to achieve high-resolution imaging of colloidal platinum nanocrystal growth. The ability to directly image and resolve critical steps at atomistic resolution provides new insights into colloidal nanocrystal growth.

Control of nanocrystal interaction and drying condition of solvent determines the final morphology of nanocrystal self-assembly. Chapter 2 presents direct imaging of nanocrystal motions in solution and real-time formation of two-dimensional nanocrystal superlattices by using liquid phase transmission electron microscopy. Nucleation and growth processes are introduced accompanying with detailed mechanistic steps and

single particle trajectories. The important role of solvent fluctuation for self-assembly of nanocrystals is explored in experiment and coarse-grained lattice gas modeling.

Concluding remarks are presented in Chapter 3.

Table of Contents

List of figures

Acknowledgements

Berkeley has surprised me through its beauty and liberty in diverse places and ideas, transformed me towards balance and independence, and challenged me to make the world a better place. I am extremely grateful to the many people who have made this experience in graduate school so incredible.

First of all, A Paul Alivisatos is an amazing advisor. He taught me to discover connections between scientific ideas, the importance of organizing those ideas into figures, and research independence. Paul's support and mentorship have opened the door to numerous opportunities, showing me a world full of possibility.

Eran Rabani, Phillip Geissler, and Alex Zettl were excellent mentors. They taught me about their respective research fields and how to think about experiments and results from different aspects of view, and helped me to write better scientific papers.

Senior members of the Alivisatos group provided great mentorship and encouragement. Haimei Zheng taught me one of the most important techniques I learned in the lab, and provided me with wise advice. Bryce Sadtler helped me think about results and new experiments. Jon Owen taught me basic skills in the wet-lab and basic questions in nano-world we think we understand but do not understand yet. Young-wook Jun taught me a great deal about general synthesis of nanocrystals. Wanli Ma, Yue Wu, Joseph Luther, Joshua Wittenberg, Cyrus Wadia, Sassan Sheikholeslami, Maxwell Merkle, Alexander Mastrorianni, Matt Sheldon, Gordana Dukovic, Prashant K. Jain, Jen Dionne, and Ming Lee Tang provided encouragement and support in the lab.

Other members of the Alivisatos group were great coworkers and friends. Emory Chan, Danny Hellebusch, Tommaso Nardi, David Britt, Debraj Ghosh, Rich Robinson, Andreu Cabot, Brandon Beberwyck, David Grauer, and Sarah Swisher showed great supports in the lab and on the soccer field. Charina Choi and Jimmy Nelson were my cohorts as we embarked on this lab voyage together. Trevor Ewers, Jessica Smith, Katie Lutker, Matt Lucas, Jessy Baker Rivest, Jesse Engel, Andrew Olson, Fadekemi Oba, Jeaneun Park, Karthish Manthiram, Noah Bronstein, Yogesh Surendranath, Kate Nichols, Somin Eunice Lee, Daeha Seo, Kathy Chia-chi Tuan, Hendrik Schlicke, Shilpa Raja, Tina Ding, Marcus Scheelle, Vivian Ferry, Jia Zhu, Linyou Cao, Na Liu, and Weilin Xu provided additional encouragement and made the lab a fun and collaborative place to work.

Kwan Pyo Kim, Jongmin Yuk, Hans Olof Elmlund, Peter Ercius, and Won Chul Lee provided additional support through scientific discussion and collaborations.

Rita Tidwell, James Wang, Karen Sharp, and Melanie Kincaid, ensured that the lab ran smoothly and that supplies for experiments were always available.

My family was crucial to the success of this endeavor. Cheolgyu Park and Kyeongsim Choi, my dad and mom, taught me what is important in life, and have given me so many opportunities to pursue my dreams. Woojung Park, my brother, has been my best friend since he was born. He supports me in life every day and I am thankful we ended up living in Berkeley together. Junghee Han, my girl friend and a future wife, is the best

partner in life I could imagine. Her insight, love, and encouragement make life an exciting adventure full of joy and happiness.

Chapter 1.

High-Resolution Observation of Colloidal Nanocrystal Growth Mechanisms using Graphene Liquid Cells

Reproduced in part with permission from: Jungwon Park, Jong Min Yuk, Peter Ercius, Kwanpyo Kim, Daniel J. Hellebusch, Michael F. Crommie, Jeong Yong Lee, A. Zettl, and A. Paul Alivisatos, "High-Resolution EM of Colloidal Nanocrystal Growth Using Graphene Liquid Cells" Science **2012**, *336*, pp 61-64.

1.1 Introduction

A wide range of physical, chemical, and biological phenomena that take place in liquids on the nanometer scale would benefit from observations with atomic resolution transmission electron microscopy. Yet it is only very recently that the powerful methods of electron microscopy have begun to be applied to imaging in liquids. Electron microscopy such as conventional transmission electron microscopy (CTEM), scanning transmission electron microscopy (STEM), and 4-D electron microscopy have long enabled direct observation of solid phase phenomena with atomic resolution.[1-4] Applying these high-powered imaging tools to study liquid phase phenomena requires more consideration to maintain realistic conditions of the liquid specimen. For example, TEM requires high vacuum and uses a high-energy electron beam, which under certain conditions can be expected to induce rapid evaporation or damage to liquid samples. In early studies, these undesired effects were partially mitigated by environmental cells that contain a reservoir with a viewing window fabricated from Si_3N_4 or SiO_2 to mimic realistic liquid conditions during TEM observation.[5-10] To date, these early liquid cells have enabled studies of nanoscale phenomena in liquids at resolutions of a few nm. Unfortunately, the relatively thick (tens to a hundred nm) and relatively high *Z* element windows in these specialized cells have poor electron transmittance, resulting in significant reduction of resolution and signal-to-noise ratio due to electron scattering, so that to date no liquid cell observations have been performed at atomic resolution.

An example of the benefits that could arise from atomic resolution in liquid cell studies arises in the growth of colloidal inorganic nanocrystals(NCs), such as Pt. The first movies of colloidal NC growth, restricted to lower resolution, revealed unexpected phenomena, namely that the colloidal Pt particles grow by frequent particle coalescence events, and most surprising, that the particle growth apparently pauses following a coalescence event. The reason for this apparent pause was attributed to possible structural rearrangements within the coalescing NCs, but this conjecture could not be proven in the earlier studies.

Recently developed protocols for the high-yield fabrication of nanometer-thick suspended membranes such as graphene, graphene oxide, and boron nitride, have provided the ultimate transparent sample supports for electron microscopy.[11-17] One carbon atom (Z=6) thick, graphene is the thinnest of these membranes. When used as a

support for TEM specimens, graphene provides a high contrast for any type of material including isolated light atoms and organic molecules. Moreover, it is straightforward to use graphene membranes to encapsulate gas, liquid or solid materials for ambient and vacuum condition experiments due to its high flexibility, mechanical tensile strength, and impermeability to small molecules.[18-21] In addition, graphene is also an excellent electrical and thermal conductor and displays minimal charging and heating effects under the electron beam.[22] An inherently inert surface eliminates chemical and physical interference from the substrate. Here, we introduce the graphene liquid cell (GLC) as a real-time reaction chamber to study atom-resolved colloidal NC growth and dynamics with an aberration-corrected TEM.

1.2 Preparation of Graphene Liquid Cells

The high-resolution liquid cell is prepared by encapsulating a Pt growth solution between two laminated graphene layers suspended over holes in a conventional TEM grid. An example of the GLC is illustrated in Figure 1.1: the TEM micrograph shows the encapsulated liquid sample (area with darker contrast) trapped between two suspended graphene sheets (lighter contrast) (**Fig. 1.1a**) accompanied with an idealized illustration (**Fig. 1.1b**). Graphene is grown on a copper foil substrate via chemical vapor deposition (CVD) and then directly transferred onto a gold TEM mesh with a perforated amorphous carbon (a-C) support.[23, 24] We prepare a stock Pt growth solution by dissolving molecular Pt precursors ($Pt(acetylacetonate)_2$, 10 mg) in a mixture of *o*-dichlorobenzene and oleylamine (9:1 in volume ratio, 1 mL total). The stock solution is pipetted directly atop two opposite-facing graphene-coated TEM grids (**Fig. 1.2a**). Upon wetting the system, the solution wicks between the graphene and a-C layers allowing one of the graphene membranes to detach from its associated TEM grid.[25] Since the van der Waals interaction between graphene sheets is relatively strong liquid droplets of various thickness from 6-200 nm can be securely trapped between a double membrane liquid pocket or blister (**Fig. 1.1**, **1.2b**, and **1.3**). Large surface strain imposed upon the detached graphene by the solution can also cause the edge of the graphene sheet to curl upon itself many times creating a nanoscroll, thus creating, if desired, multi-membrane protected liquid pockets (inset of **Fig. 1.2b**). Generally, for our GLCs graphene remains fully intact throughout the fabrication process as indicated by a relatively low defect-induced graphene D peak (around 1350 cm^{-1}) observed in Raman spectra (**Fig. 1.4**).

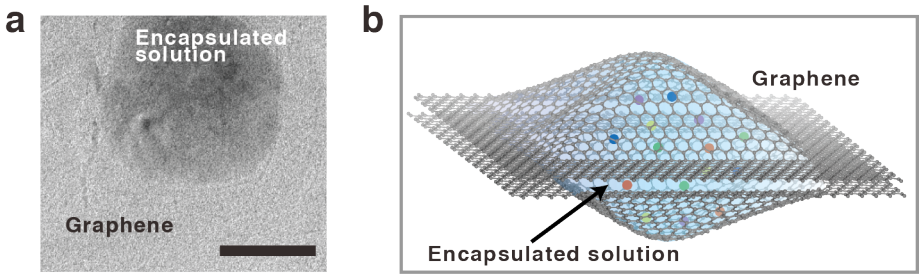

Figure 1.1. Graphene liquid cell (GLC). **(a)** TEM image of a GLC; laminated graphene layers immobilize a blister of encapsulated stock solution (dark region). Scale bar represents 50 nm. **(b)** Idealized illustration of local GLC encapsulating growth solution.

We image Pt NC growth and dynamics in as-prepared GLCs on the TEAM I (Transmission Electron Aberration-corrected Microscope I) managed by the National Center for Electron Microscopy. The microscope is operated at 80 kV with a beam intensity of 10^3 to 10^4 A/m^2 maintained during NC growth. Upon locating a liquid pocket on the TEM grid, the beam intensity is increased, which reduces the Pt precursor and initiates NC growth. The graphene membrane with encapsulated liquid remains intact over the entire desired time period of TEM observation ensuring prolonged high-resolution *in-situ* imaging. Spherical and chromatic aberration correctors on TEAM I further contribute to the exceptionally high-resolution and enhanced signal-to-noise ratio.

a (i) Two graphene deposited TEM grids are superimposed.

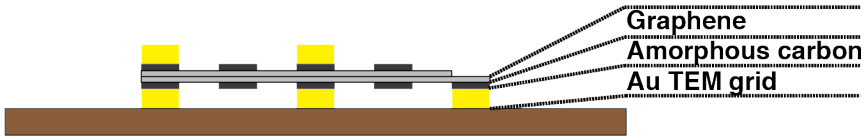

(ii) Extra Pt growth solution is removed by suction after dropping.

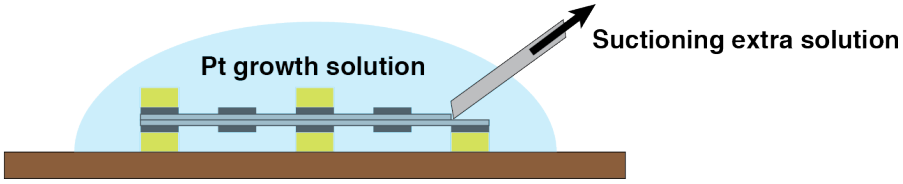

(iii) Pt growth solution is entrapped between two graphene membranes after drying.

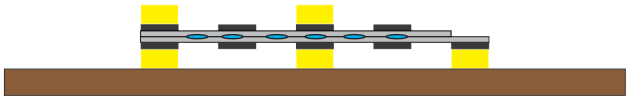

(iv) Top TEM grid is removed.

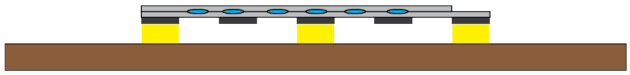

b

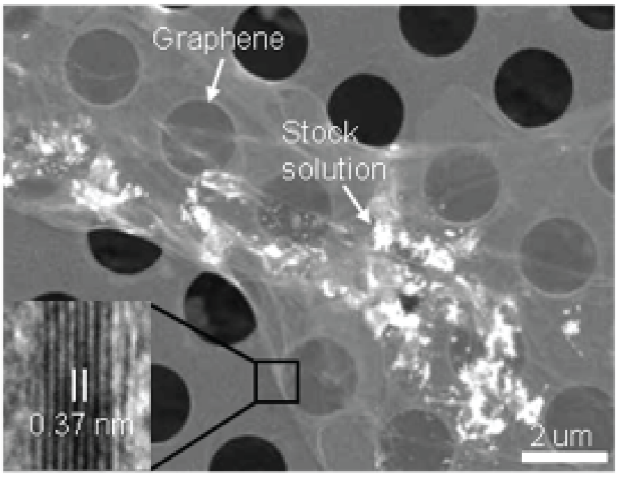

Figure 1.2. Preparation of a graphene liquid cell. **(a)** Illustration of the fabrication processes of the graphene liquid cell. **(b)** SEM image of a graphene liquid cell. The inset is a TEM image of a nine-layered graphene on edge; that the distance between adjacent graphene layers is 0.37 nm.

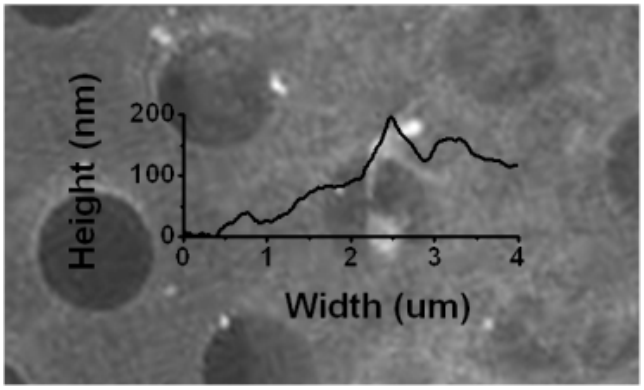

Figure 1.3. AFM image and height profile of a GLC supported on a holey a-C grid. Encapsulated Pt growth solution appears white in the image and yields a spike in the height profile.

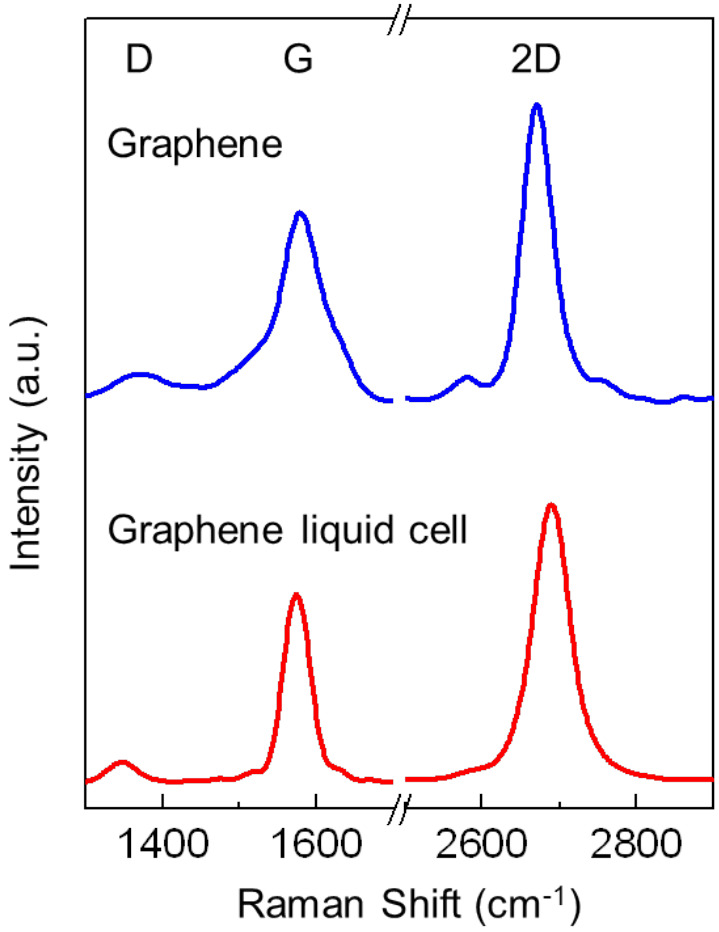

Figure 1.4. Raman spectra of graphene deposited on TEM grid and graphene liquid cell.

1.3 Diffusion of Nanocrystals in Liquid Encapsulated in Graphene Liquid Cells

Extended movies of colloidal Pt NC growth (not included in this dissertation) reveal major differences between data collected using GLCs compared to previous cells with silicon nitride windows even at the earliest stages of the colloidal Pt NC growth. It is possible to clearly discern colloidal Pt NCs as small as 0.1 nm radius and to track their motion. Using silicon nitride window cells, the NC motion is severely perturbed by the windows; NCs of Au and Pt in such cells have been observed to remain localized close to one of the windows, weakly bound to the surface layer, and to execute complex non-Brownian motion near the window.[9, 10] In contrast, the interaction of the NCs with graphene is very weak, and the motion of the colloidal Pt NCs is not corrupted by association with the window. Two-dimensionally projected positions for a single NC trajectory are tracked as it grows from 0.28 to 0.55 nm in radius by monomer attachment. As it grows, the particle diffusion slows as expected for Brownian motion (in the SiN cell the diffusivity does not scale this way due to substrate interactions). The trajectory is divided into three equal parts based on time. As the NC grows with time, the mean square displacement (MSD) $\langle x^2 \rangle$ decreases (**Fig. 1.5a**). Representative TEM images of the NC at each time frame are displayed in **Fig. 1.5b** with color gradient mapped images for clarification. The two-dimensional diffusivity D is extracted from the slope of the MSD as a function of time; the corresponding NC size is averaged for each time regime. **Figure 1.5c** shows that the measured D of a NC decreases monotonically as the NC steadily grows. One similarity with previous tracking studies in the silicon nitride window cells is that the NC diffusivities in the confined liquid are found to be smaller than those expected from the bulk liquid viscosity.

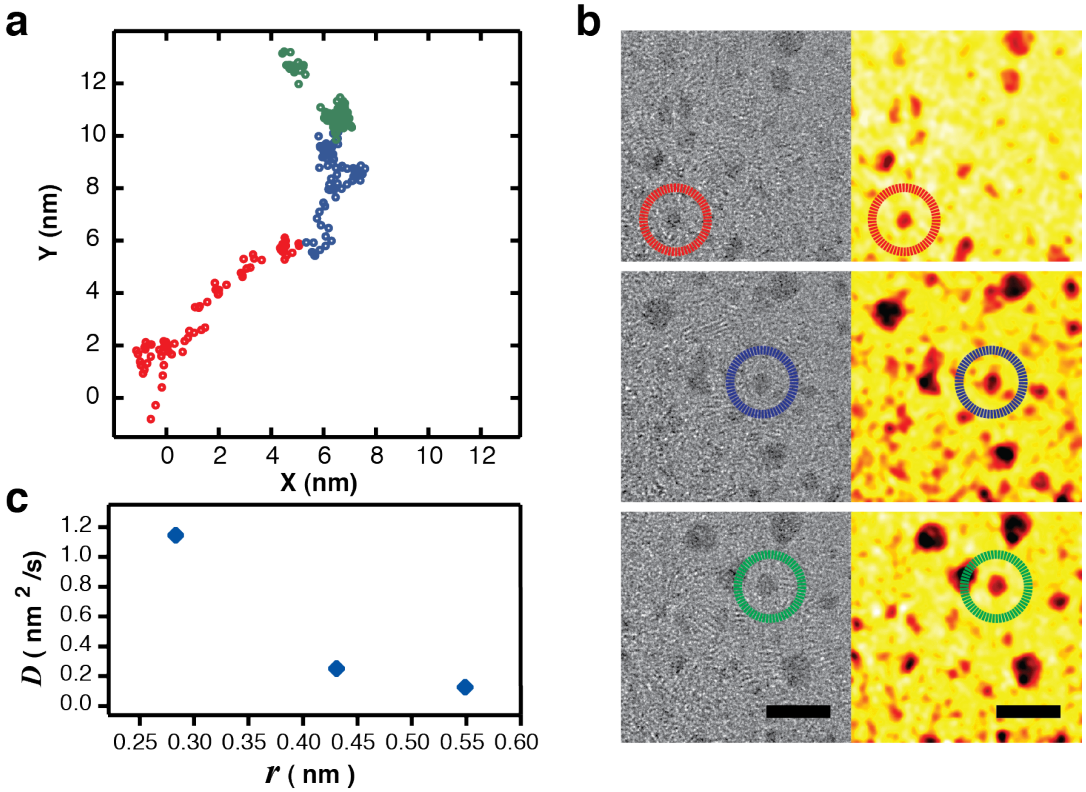

Figure 1.5. Tracking of NC position and measured diffusivity with average size from 0.28 nm to 0.55 nm in radius during growth. **(a)** Positions of a NC in consecutive time regimes of 20 seconds each during growth: red, blue, and green colors indicate the earliest to final time regime, respectively. **(b)** Representative TEM images of the tracked NC in the different time regimes. Colors of the circles match the time regimes in (A). The panels on the right are false-color representations of the TEM contrast data. Scale bars represent 5 nm. **(c)** Diffusivity *D* as a function of average NC radius (*r*) over the 20 seconds of each regime.

1.4 Coalescence on Preferred Crystal Orientation for the Growth of Nanocrystals

The NCs grow both by monomer addition and by frequent coalescence events (**Fig. A1.1**).[10, 26, 27] Using the GLC, it is possible to directly observe critically important features of the coalescence process that could not be resolved in earlier studies (TEM images of Pt NCs in the final stage of the growth in GLCs can be found in **Fig. A1.2** and **A1.3**). We first examine the crystallographic orientation relationship of NCs during their coalescence. **Figure 1.6** shows TEM images of *in-situ* Pt NC growth by coalescence. Incoming small NCs are marked with white arrows on TEM images and can be seen clearly in black/white color mapped insets. Once NCs collide at {111} planes, they merge

quickly, within 0.26 seconds (the limit of our acquisition time). We observe that most coalescence events proceed along the same crystallographic direction indicating that there is a specific NC orientation for coalescence. This result is remarkable, since {111} planes of a face-centered cubic crystal have the lowest surface energy. This behavior may be due to different degrees of ligand coverage on different NC factes; {111} planes of a face-centered cubic crystal have the lowest surface energy and therefore perhaps the lowest ligand coverage.[28, 29] In this scenario, NCs that contact at {111} planes experience minimal ligand obstruction and therefore quickly unify to minimize the total surface area—and thus overall surface energy. Coalescence in this manner proceeds in one of two ways: contact which joins identical, or mirror, {111} planes. NCs captured in Fig. 6A exemplify the first instance, which results in a perfectly aligned crystal with a single crystallographic domain as shown in the fast-Fourier transformed (FFT) pattern. The second case, as seen in **Fig. 1.6b** and **1.6c** yields NCs with a twin boundary; the corresponding FFTs reveal two double domains. For the duration of our movies, twin boundaries formed from coalescence remain locked within the NC. The interface energy of the twin boundary is known to be thermodynamically non-negligible. However, it appears that, under the present experimental conditions, structural rearrangements of the NCs occur mainly by surface rearrangements and not by reorganization of the complete NC interior. Mis-oriented particle coalescence appears to account for the formation mechanism of twin boundaries commonly observed in synthesized face-centered cubic metal NCs.[29]

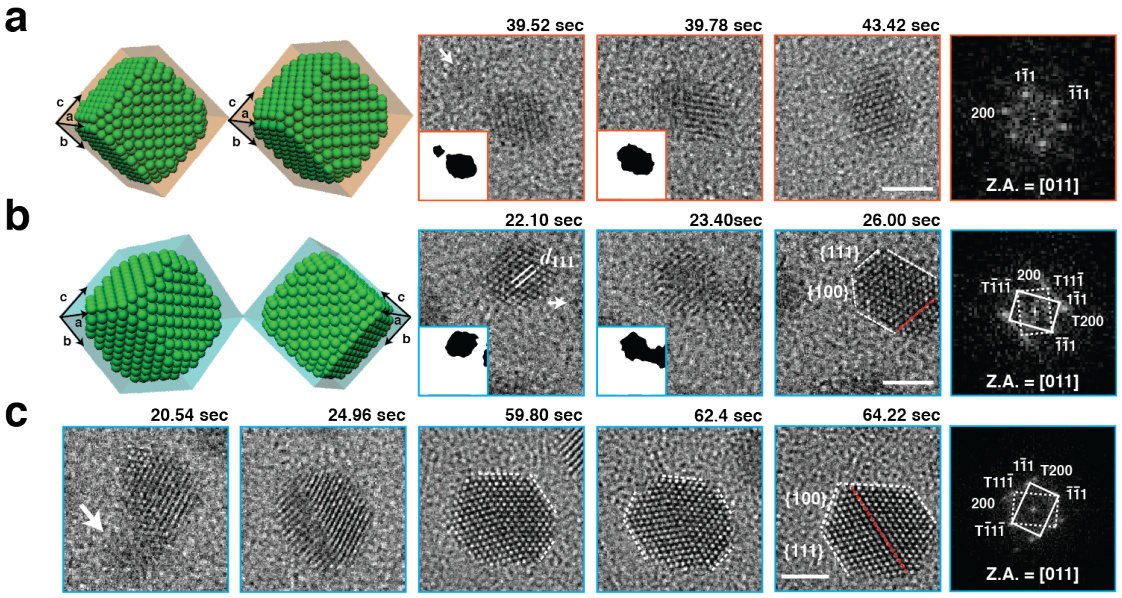

Figure 1.6. Still snapshots of Pt NC growth via coalescence and crystal structure evolution observed with atomic resolution in a GLC. Schematic illustrations and corresponding TEM images exhibiting NC coalescence along <111> directions which evolve into **(a)** a single crystalline face-centered cubic structure or **(b)** a twinned face-centered cubic structure. Black and white insets represent scaled down NC volume projections and background, respectively, to clarify the NC shapes and positions. **(c)** Shape evolution of the Pt NC by straightening of the twin boundary and evolution towards a hexagonal shape consistent with the Wulff construction. These reconstructions are consistent with surface rearrangements. For (A)-(C), FFT images of the final frame are provided at the end of each sequence. Arrows point out incoming NCs. Scale bars are 2 nm and zone axis abbreviated as Z.A.

1.5 Structural Reorganization during Nanocrystal Coalescences

Before coalescing along the {111} orientation, the NCs exhibit a prolonged period of correlated motion that facilitates lattice alignment and unification. We track size (blue and green in **Fig. 1.7a**) and position change (**Fig. 1.7b** and **Fig. A1.4**) of two NCs before they coalesce at the sub-nanometer range. In **Fig. 1.7a**, two NCs show correlated rather than independent motion over a 100 second interval, culminating in lattice alignment and coalescence. The correlated motion presumably arises because of inter-particle attractive forces. Based on theoretical studies, the attractive forces can be attributed to van der

Waals interactions, steric repulsions, and depletion forces arising from surface ligands. The duration of the correlated motions we observe in TEM movies vary depending on NC size and the local thickness of the liquid medium. We measure the center-to-center distance (red in **Fig. 1.7a**) between two adjacent NCs from a position plot of the two NCs (**Fig. 1.7b**). Comparing this distance with NC size provides insight into the mechanisms of NC growth by coalescence. As the freely moving NCs draw close, the center-to-center distance rapidly decreases. This initial event occurs within 40 sec (see **Fig. 1.7a**). The center-to-center separation fluctuates between 4 to 6 nm for the next 25 sec. While this dynamic event proceeds, the NCs also grow in size from around 0.75 nm to 1 nm in diameter due to monomer addition. The surface ligand, oleylamine, is known to be 1 to 2 nm long depending on the orientation and extension of its floppy alkyl chain and surface packing density. Therefore, the sustained correlated motion occurs with weakly touching surface ligand layers. The center-to-center distance shows even more confined fluctuation of about 1 nm in the time interval from 80 to 130 sec. In this time range we observe from **Fig. 1.7a** that the correlated motion of the two NCs exhibits three-dimensional behavior of rolling and relative sliding of NCs over each other. Throughout this period the NCs continue to grow by monomer addition, continuously increasing the attractive force between the particles. After 130 sec, the center-to-center distance approaches the sum of the radii of the two NCs and the NCs lattices align, leading to coalescence at 160 sec.

Single particle growth trajectories in the one previous lower-resolution study of Pt NC growth showed an apparent size decrease after coalescence, as well as a short pause following coalescence before apparent growth by monomer attachment has resumed (**Fig. A1.1**).[10] In the GLC, it is possible to examine and understand in much more detail these unexpected phenomena that follow NC coalescence. **Figure 1.7c** plots the change in length (*l*, along the center-to-center direction), thickness (*t*, vertical direction to the length), and neck diameter (*n*) of the coalesced NCs, while **Fig. 1.7d** shows the corresponding TEM images. The NCs are connected together by a neck at the initial stage of coalescence. Neck growth is accompanied by a decrease in *l* and *t*. This indicates that the atoms migrate to the neck region by surface diffusion.[30] Following coalescence, the NC structure also gradually reorganizes, evolving truncated surfaces. Returning to **Fig. 1.6c**, the NC shape after coalescence changes from quasi-spherical to a hexagonal shape that minimize the surface energy of NC as expected from a Wulff construction, also by surface diffusion processes.

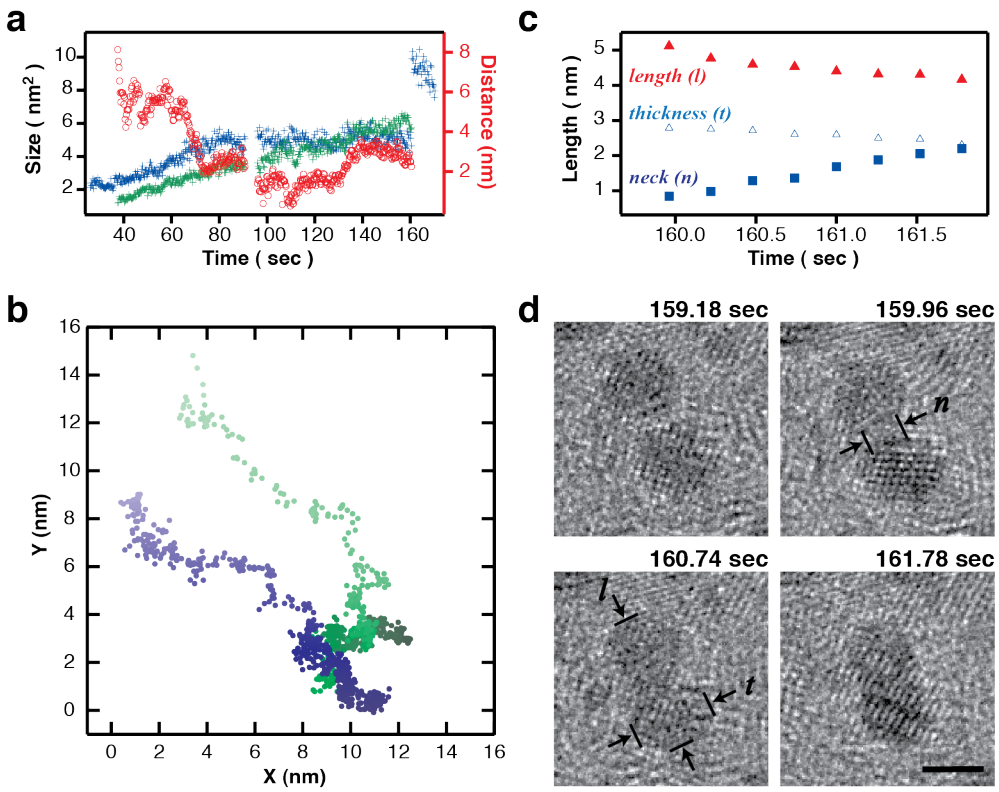

Figure 1.7. Pt NC dynamics before (a, b) and after coalescence (c, d). **(a)** Projected distance between two NCs (red) up until the two NCs coalesce, as well as the size (blue and green, area (nm^2) is measured for spherical and ellipsoidal NC shapes before and after coalescence, respectively) of the two NCs during the period of correlated motion. The NC labeled in green merges with the blue-labeled NC at 160 sec. Structural reorganization is tracked with atomic resolution after the coalescence event. (Two consecutive movie clips were merged into Movie S1, accounting for the data gap of 5 sec at the 95 sec point.) **(b)** Two-dimensional projected position change of the two NCs before coalescence. Blue and green colors correspond to the NCs in (A). Color gradient is used to represent time eolution from 40 sec (bright color) to 160 sec (dark color). **(c)** Neck diameter (*n*), thickness (*t*), and length (*l*) after the coalescence of the two NCs as a function of time. Time domain of this plot corresponds to the interval the apparent NC size decreases after coalescence in (A). **(d)** Still snapshots from a movie showing neck formation during coalescence and shape evolution into an ellipsoid by neck filling and length reduction of the NC. Scale bar represents 2 nm.

Chapter 2.

Direct Observation of Nanocrystal Superlattice Formation by Using Liquid Cell Transmission Electron Microscopy

2.1 Introduction

Nanocrystals (NCs), also known as artificial atoms, provide an ideal model system to study crystallization at the nanometer scale and above. This is because their physical properties can be tuned by changing their composition, size, and surface ligand, allowing for control over the interparticle interactions. This offers an opportunity to uncover the interplay between entropic and enthalpic effects in the self-assembly process and perhaps, provide the necessary insights that would help guide the creation of large scale arrays suitable for future energy harvesting and optoelectronic device applications that rely on the bottom-up approach.[31-34] Understanding the phase behavior of colloidal NC solutions from dispersions to two- and three-dimensional solids has considerable fundamental and practical importance.

Most NC assemblies, however, are formed under empirically optimized, perhaps uncontrolled, drying conditions.[35-51] Experimental studies of the fundamental mechanisms of assembly formation are very desirable since the final morphologies are very sensitive to different crystallization conditions including size, shape, solubility and surface ligand of the NCs, the evaporation rate of the solvent, inter-particle interactions, and particle-substrate interactions.[52-55] The lack of such studies is even more notable in view of recent theoretical progress based on the Dzyaloshinskii-Lifshitz-Potaevskii model, the coupled-dipole method, and the coarse-grained lattice-gas models.[56-61] These have sought to explain how interactions among NCs and solvent fluctuations affect final assembled structures, yet many of the predictions await experimental assessment.[62-66]

In-situ optical microscopy was used successfully to quantify the real time and real space crystallization and melting of colloidal polystyrene microshperes, providing great insight into the forces between the particles and the factors influencing crystallization and melting.[67-80] In NC assembly, where the size domain is below the diffraction limit of visible light, in-situ atomic force microscopy, optical microscopy, and small angle X-ray scattering have been the leading tools to study the nucleation and growth of NC clusters and the formation of superlattices at liquid/air and liquid/substrate interfaces.[81-88] However, microscopic details of how single NCs position at potential lattice points of a growing superlattice remain elusive. With the recent development of in-situ liquid cells

for transmission electron microscopy (TEM), it is now possible to extend these studies down to the nanoscale.[9, 10]

In this work, we employed liquid-phase TEM and observed the formation of Pt NC assemblies, in-situ, at the substrate/solvent/vacuum interface. The technique provides means to follow individual NC trajectories and to study in depth the evolution of the system to an ordered assembled state in real time. We demonstrate that during assembly, Pt NCs were mainly driven by the strong capillary force of the evaporating solvent front.[89] We find that the assembly proceeds by several distinct steps. In the first, NCs are contracted and condensed by the rapidly moving solvent into amorphous agglomerates, which span several monolayers in thickness. These agglomerates then expand and flatten to a single NC thickness. At this point, local fluctuations allow the system to relax to an ordered superstructure. These domains then grow by the subsequent addition of NCs, where capillary forces play an important role as well. Coarse-grained modeling provides a consistent picture with these experiments.

2.2 Micro-Fabrication of Liquid Cells and Sample Preparation

A schematic diagram of the liquid cell can be found in previous reports. Micro-fabrication processes of silicon-nitride membraned liquid TEM cells are introduced in **Fig. 2.1**. 100 μm thick silicon wafer is thermally deposited with SiNx membranes of 20 to 30 nm thickness on both sides. Photoresist deposition, photo lithography, development of photoresist, and selective Si wafer etching steps are apllied sequentially to pattern reservoirs and a electron beam transparent window for top chips and only a window for bottom chips, respectively. Indium spacer is thermally deposited and patterned to remain along edge of bottom chips. Indium spacer controlled from 20 nm to 700 nm in thickness determines the height of the loading resorvoir of liquid. Top and bottom chips are bonded to align two windows from both and baked at 100 ^{o}C for two or three hours.

Pt NCs were prepared by reduction reaction of molecular platinum ion precursors following previously reported method with modification.[90-91] A total of 0.05 mmol of Pt ions ($(NH4)_2Pt(IV)Cl_6$: 80% and $(NH4)_2Pt(II)Cl_4$: 20%), 0.75 mmol of tetramethylammonium bromide, and 1.00 mmol of poly(vinylpyrrolidone) (in terms of the repeating unit; *M*w 29 000) were dissolved into 10 mL of ethylene glycol in a 25 mL round-bottom flask at room temperature. This solution was heated to 180 °C in an oil bath at 60 °C/min and kept at 180 °C for 20 min under argon flow and magnetic stirring. After formation of dark brown solution, it was cooled to room temperature. Acetone (90 mL) was added and black suspension was separated by centrifugation at 3000 rpm for 10 min. The black product was re-dispersed in 20 mL of ethanol and precipitated by adding excess amount of hexane. This cleaning process was repeated two or three times. Resulting Pt NCs were dispersed in excess amount of oleylamine for further ligand exchange reaction and refluxed overnight in an oil bath under mild stirring. NCs were separated from the solution by centrifugation at 14000 rpm for 30 min. Obtained Pt NCs were soluble in organic solvents. For in-situ liquid cell experiment, here, Pt NCs were

dispersed in organic solvent mixture (*o*-dichlorobenzene : pentadecane : oleylamine = 100 : 25 : 1 in volume ratio). As-prepared Pt NCs solution in solvent mixture was loaded into two reservoirs of liquid cell by micro-pipette. Liquid sample was exposed ambient condition for a while to ensure that *o*-dichlorobenzene dries out before sealing. Vacuum grease was applied on one side of copper aperture grid with a hole size of 600 micrometers. Liquid cell was covered with vacuum grease applied aperture grid for airtight environment. Such procedure provides approximately 30 minutes of viewing time.

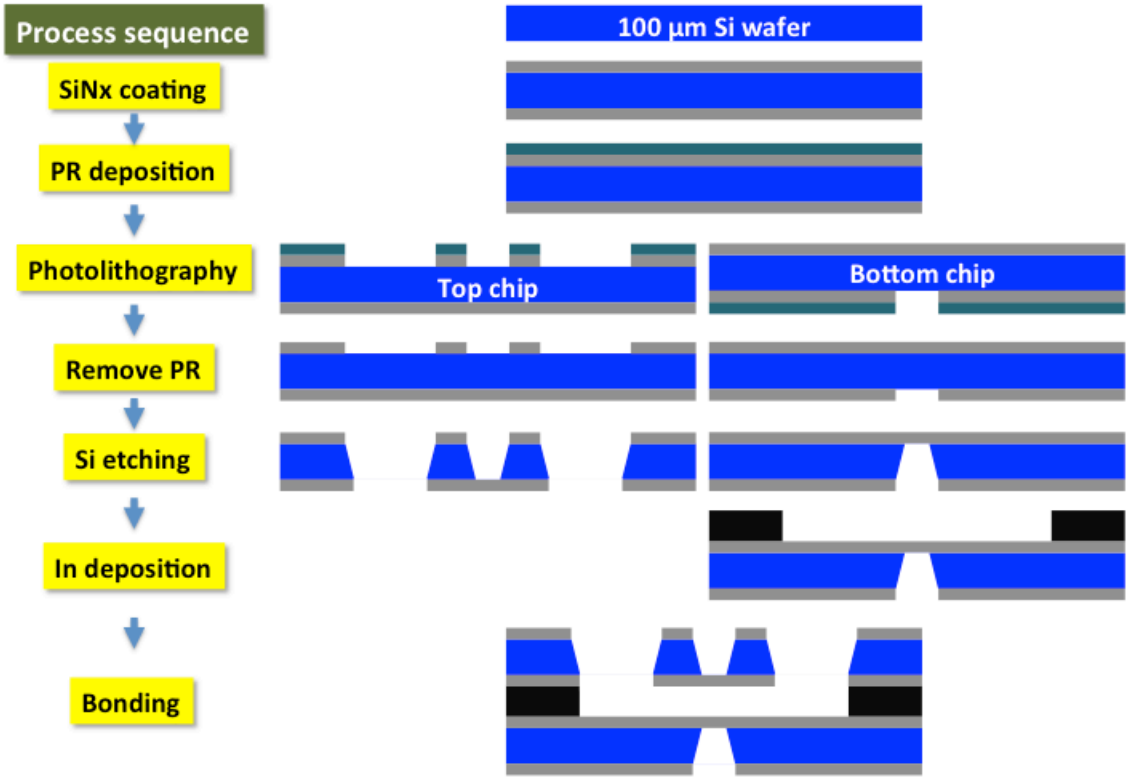

Figure 2.1. Fabrication processes of silicon nitride membrane liquid TEM cells.

2.3 Coarse- Grained Lattice Gas Simulation

Simulations have been performed in 3D with a lattice gas Hamiltonian defined by:

$$H = -\varepsilon_\ell \sum_{ij} \ell_i \ell_j - \varepsilon_n \sum_{ij} n_i n_j - \varepsilon_{n\ell} \sum_{ij} n_i \ell_j - \varepsilon_{\ell s} \sum_{ij} \ell_i s_j - \varepsilon_{ns} \sum_{ij} n_i s_j - \mu \sum \ell_i,$$

where the sums run only over nearest neighbors on a rectangular 3D lattice, ℓ_i, n_i, and s_j are binary variables roughly proportional to the density of the solvent, nanoparticles and

substrate at site i, respectively (0 for low density or 1 for high density). ε_ℓ, ε_n, $\varepsilon_{n\ell}$, $\varepsilon_{\ell s}$, and ε_{ns} are the liquid-liquid, NC-NC, liquid-NC, liquid-substrate, NC-substrate interfacial energies, respectively.[60-62, 92-94]

The specific choice of interaction parameters follows the guidelines described in our previous work. To prevent aggregation of nanoparticles in the presence of the liquid, we take $\varepsilon_\ell < \varepsilon_{n\ell}$. In addition, the attraction between the nanoparticles is taken to be larger than the attraction between the nanoparticles and the liquid, i.e., $\varepsilon_{n\ell} < \varepsilon_n$, so that the nanoparticles tend to aggregate in the absence of liquid. More specifically, we set $\varepsilon_{n\ell} = \frac{3}{2}\varepsilon_\ell$ and $\varepsilon_n = 2\varepsilon_\ell$ in all the results reported in this work.

The last term in the above equation represents the chemical potential, μ, and is used to establish the average concentration of liquid and vapor cells at equilibrium. A large negative value of μ will favor evaporation, while positive values will favor wetting. The crossover from wetting to evaporation occurs at $\mu = -3\varepsilon_\ell$ for the present model. Since the vapor pressure of the nanoparticles and the substrate is negligibly small, we do not include a chemical potential for these species in the Hamiltonian. In other words, the binary variables associated with the nanoparticles and the substrate (n_i and s_i, respectively) conserve the corresponding densities (conserved order parameter), while the binary variable representing the liquid does not conserve density (nonconserved order parameter).

The dynamics are stochastic both for solvent density fluctuations and for NC diffusion, where balance is preserved. The NCs undergo a random walk on the three dimensional lattice, biased by their interactions with each other, with liquid cells, and with the substrate. The diffusion rate is controlled by how often we attempt to displace the nanoparticles compared to the solvent moves (defined below). In detail, we attempt to displace a NC by single lattice spacing in a random direction every N_ℓ solvent moves, but only if the region into which the nanoparticle moves is completely filled with liquid. To maintain solvent density, the void cells left behind the moving nanoparticle are filled with liquid, compensating for the liquid cells overtaken by the nanoparticle in its move. Thus, the nanoparticle moves can be considered as swapping locations between the nanoparticle and the adjacent liquid cells which it displaces. This constraint mimics the very low mobility of NCs on a dry surface. It also provides an additional coupling between the kinetics of evaporation and nanoparticle phase separation. Such a move is accepted with the Metropolis probability:

$$P_{acc} = \min[1, \exp(-\beta \Delta H)],$$

where β is the inverse temperature and ΔH is the energy difference between the new and old configuration. To mimic the low mobility of NCs we choose a large value for N_ℓ (typically 3 orders of magnitude larger than our previous simulations).

In our original work, liquid moves where quite simple. We attempted to convert a randomly chosen lattice cell i that is not occupied by a nanoparticle or the substrate, from liquid to vapor (or from vapor to liquid), $\ell_i \to 1 - \ell_i$ only if at least one of the adjacent lattice cells, j, contains vapor, i.e., if it satisfies $\ell_j + s_j + n_j = 0$). This constraint is

applied to both condensation and evaporation to ensure that balance is retained. The direct outcome of this constraint is that evaporation occurs layer by layer (although not necessarily homogeneously for each layer), and the formation of bubbles (i.e., boiling) is practically never observed. In addition, this constraint also inhibits the formation of configurations, where nanoparticles that are located far from the substrate become surrounded only by vapor cells. The solvent moves are then accepted with the above Metropolis probability, $P_{acc} = \min[1, \exp(-\beta\Delta H)]$.

In the present study, liquid moves are more evolved to include, in a primitive way, "dragging" of the NCs by the receding solvent front. We attempt the same evaporation move described above. However, in addition, if at least one of the neighboring cells is occupied by NCs, we attempt to "drag" the NC in the opposite direction or in the direction of the cell i, depending on whether cell i was filled with liquid or not, respectively, but only if the region into which the NC moves is filled with liquid (as before Solvent density in lattice cells overtaken by this displacement is regenerated in the wake of the moving nanoparticle.). The probability to attempt to drag the NC is given by ξ (i.e. not every evaporation move includes a dragging attempt, for the results described in this work $\xi = 0.001$). In the case that an evaporation move is followed by a dragging move, the Metropolis probability needs to include also the Hastings proposal density:

$$P_{acc} = \begin{cases} \ell_{\mathrm{i}} = 1 & \min[1, \exp(-\beta\Delta H)\frac{n}{\bar{n}}] \\ \ell_{\mathrm{i}} = 0 & \min[1, \exp(-\beta\Delta H)\frac{\bar{n}}{n}] \end{cases},$$

where n is the number of NC adjacent to cell i and $\bar{n}$ the number of NC that are allowed to move. Similarly, reverse moves are included for condensation with the corresponding Metropolis probability, preserving balance.

2.4 Two-Step Nucleation of Domains in Nanocrystal Superlattice Formation

Figure 2.2 summarizes the NC assembly formation obtained from a typical in-situ liquid TEM experiment. The electron beam has been used not only as an imaging tool but also as a driving force to evaporate the solvent locally from the illuminated area. Varying solvent thicknesses induced by the electron beam radiation can be seen as change in contrast as time progresses with thinner areas appearing as lighter contrast and thicker areas appearing as darker contrast (**Fig. 2.2a**). Solvent evaporation nucleates at several spots which show up as bright circles in the first image and continue to expand until the solvent is gone in the final image. Similar patterns were observed during the evaporation of water.[95-96] We also tracked several NCs forming one large domain in the final stage. Their relative positions (corrected for thermal drift of the TEM – see SI for more details), corresponding to the red-squared area in the TEM images, are shown in **Fig. 2.2b**, **Fig. A2.1**.[97-99]

It is important to note that the length scale of the final ordered assembly is limited by the observation process, and the fact that evaporation is initiated at multiple independent sites.

Nonetheless, we can track the motion of every particle associated with one evaporation zone, and in this way decipher the critical steps of NC assembly. Assembly driven by a single larger evaporation front, such as often occurs by ordinary evaporation in lab experiments outside the TEM, would likely follow the same microscopic steps, and further evidence for this will be shown below.

The motion of the NCs was captured with camera frame speeds of five to thirty frames per second, in order to track individual NCs with adequate precision. The thickness of the liquid sample with NCs was limited to less than 100nm. Under the current experimental setup, the NC Brownian motion was significantly suppressed.[9, 10, 100, 101] The gap between two SiNx windows was controlled by the height of indium spacer during fabrication steps but the actual thickness of the liquid sample could be thinner than the desired gap size, since excess solvent (o-dichlorobenzene) was dried during the sample loading. In this regime, the NCs motion is mainly determined by the formation of drying patches.[64, 65, 100] As the drying patches expand, solvent fronts push the NCs to areas that are still wet by the solvent (**Fig. 2.2**). The inter-particle distance continuously decreases until NCs eventually pack together in an ordered 2D phase (**Figs. 2.2a** and **2.2b**).

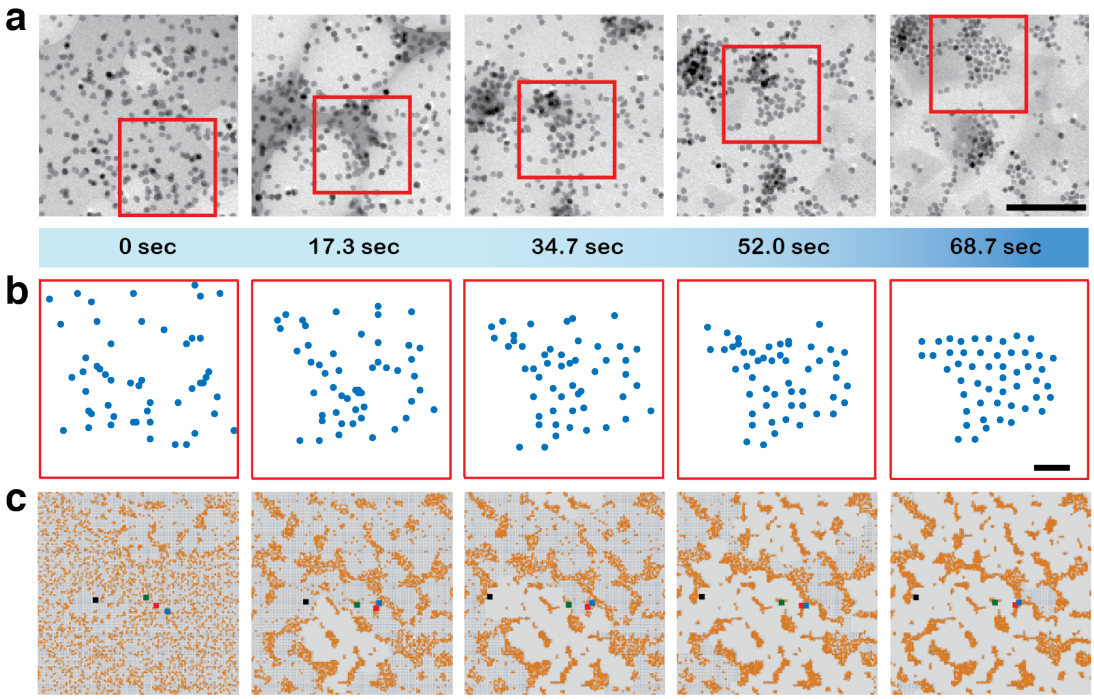

Figure 2.2. In-situ observation of superlattice formation by liquid phase TEM and lattice gas modeling. **(a)** TEM snapshots from Movie 1 at different times. The scale bar is 100 nm. **(b)** Relative positions (corrected for thermal drift of the TEM sample) of selected 51 NCs taken from the red-squared area (120 nm x 120 nm) in Fig. 1a. The scale bar is 20 nm. **(c)** Top view of assembly formation obtained from lattice gas modeling. Selected NCs are enlarged and colored with black, green, red, and blue to signify their motion Time from left to right correspond to 15000, 25000, 25600, 26400, and 27000 in Monte Carlo (MC) units, respectively for coverage $\rho = 30\%$, chemical potential $\mu = -3\frac{1}{4}\varepsilon_\ell$, temperature $T = \varepsilon_\ell$, and interfacial energies $\varepsilon_{ns} = 1\frac{1}{2}\varepsilon_\ell$, $\varepsilon_{\ell s} = \varepsilon_\ell$, and $\varepsilon_n = 2\varepsilon_\ell$. Image size corresponds to approximately 200×200 nm^2.

This picture is also consistent with lattice-gas simulation results shown in **Fig. 2.2c** (see also **Fig. A2.2** and **Fig. A2.3**) under low NC diffusivity, where in addition to diffusive motion, NCs can also move as a result of solvent dragging. The results shown in Fig. 9c illustrate several important points. In the limit where the self-assembled structures are determined by solvent fluctuations, dragging can provide a competing mechanism for NC assembly, even when the NC diffusivity is rather low. The resemblance between the final morphologies obtained here and our previous simulations which ignored dragging (not shown) is rather striking (see also **Fig. 2.4** for the experimental comparison). Despite the fact that in the absence of evaporation the NCs' mean square displacement (MSD) is quite low, dragging can move the NCs on length- and time-scales relevant for self-assembly, moving the particles across the detection window as they meet to form an ordered domain. The correlation between the morphologies obtained by the TEM

experiments and the coarse-grained simulations further supports the importance of solvent dragging.

For each frame in **Fig. 2.2a**, we selected 51 NCs (same particles as in **Fig. 2.2b**) forming one large domain at the final assembly stage and calculated their two-dimensional projected surface coverage within the minimum convex polygonal area containing all the selected NCs. In **Fig. 2.3** we show typical coverage plots corresponding to the trajectory shown in Fig. 9b. The behavior of the surface coverage of NCs can be divided into four regimes (1st: 0 sec to 20 sec, 2nd: 20 sec to 40 sec, 3rd: 40 sec to 58 sec, and 4th: 58 sec to 68.7 sec). In the first stage, the inter-particle distance decreases as NCs are dragged together by the evaporating solvent front. However, the rate of evaporation is retarded due to capillary condensation in the second stage. As the inter-particle distance decreases, the solvent trapped between NCs exposes less surface to the atmosphere and evaporates more slowly. This leads to a retarded evaporation rate resulting in a slower increase of density in the second stage. During the third stage, density reaches its maximum level which indicates that the NCs have condensed, containing multiple layers of NCs. Upon completion of evaporation in the fourth regime, these multiple layers flatten out into ordered domains while maintaining maximum level of surface coverage. During the very last stage of assembly formation, solvent fluctuations compress the NCs onto the substrate to form a stable superlattice as the solvent dries completely.

In **Fig. 2.3** we also plot the 2D bond orientational order parameter as a function of time for the same trajectory to quantify crystalline ordering of the selected NCs. The bond orientational order parameter is defined by:

$$\Psi_6 = \left| \langle \frac{1}{nn} \sum_{k=1}^{nn} \exp\left(6i\theta_{jk}\right) \rangle \right|$$

where θ_{jk} is the angle of the bond between particle *j* and its neighbor *k*, and *nn* is the number of nearest neighbors.[102-104] Nearest neighbors were defined as NCs whose inter-particle separation fell below a cutoff value that was derived from the first minimum of the radial distribution function (**Fig. A2.4**). The value of Ψ_6 is 1 for an ordered structure on a triangular lattice and near 0 for a disordered lattice. Ψ_6 shows a small fluctuation before it abruptly spikes up around 57 sec to a value of ~0.5. The maximum value of Ψ_6 at the final stage is lower than 1 due to finite size effects. The most interesting observation is the abrupt increase of Ψ_6 that occurs after the density of NCs plateaus (58 sec). This indicates that NCs form a very dense amorphous structure before crystallization. This is consistent with a two-step crystallization mechanism observed in nucleation of protein and micro-sized colloidal particles, where monomers first form an amorphous dense phase followed by crystallization.[105] A similar two-step crystallization process has been demonstrated for the self-assembly of binary mixtures within a coarse-grained model.[92]

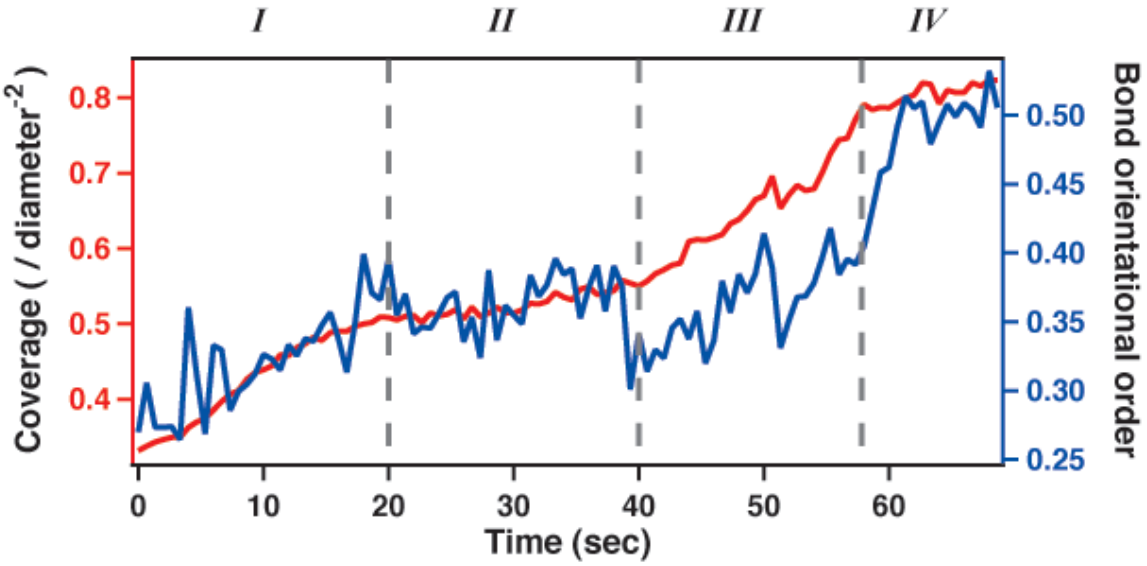

Figure 2.3. Surface coverage of NCs and the 2D bond orientational order parameter, a measure of crystalline ordering, as a function of time. Results are shown for the same trajectory of Fig. 1b.

Once under view in the TEM, the 200 kV electron beam radiation interacts strongly with the liquid. One effect we see clearly is beam-induced evaporation. Thus, a concern one may raise is related to the effects of the electron beam and TEM conditions on the self-assembly process. As a check, we have also compared the final assembled domain with superlattice structures formed by drop-casting on a SiNx membrane TEM grid. The SiNx membrane was prepared by the exact same fabrication process as for the SiNx windows of a liquid cell to ensure substrate interaction effects are identical. **Figure 2.4** compares final domains from assemblies formed under electron beam irradiation and typical superlattice patterns resulting from a drop-casting experiment. Localized and heterogeneous drying condition in TEM due to the presence of the electron beam results in a smaller length scale and less uniformity of the superlattice formed in the TEM compared to the drop-casting experiment. However, beyond similarity between overall superlattice patterns for the two cases, the identical inter-particle distance indicates that the slightly overlapping NC ligand shells remain intact (**Fig. A2.4**).

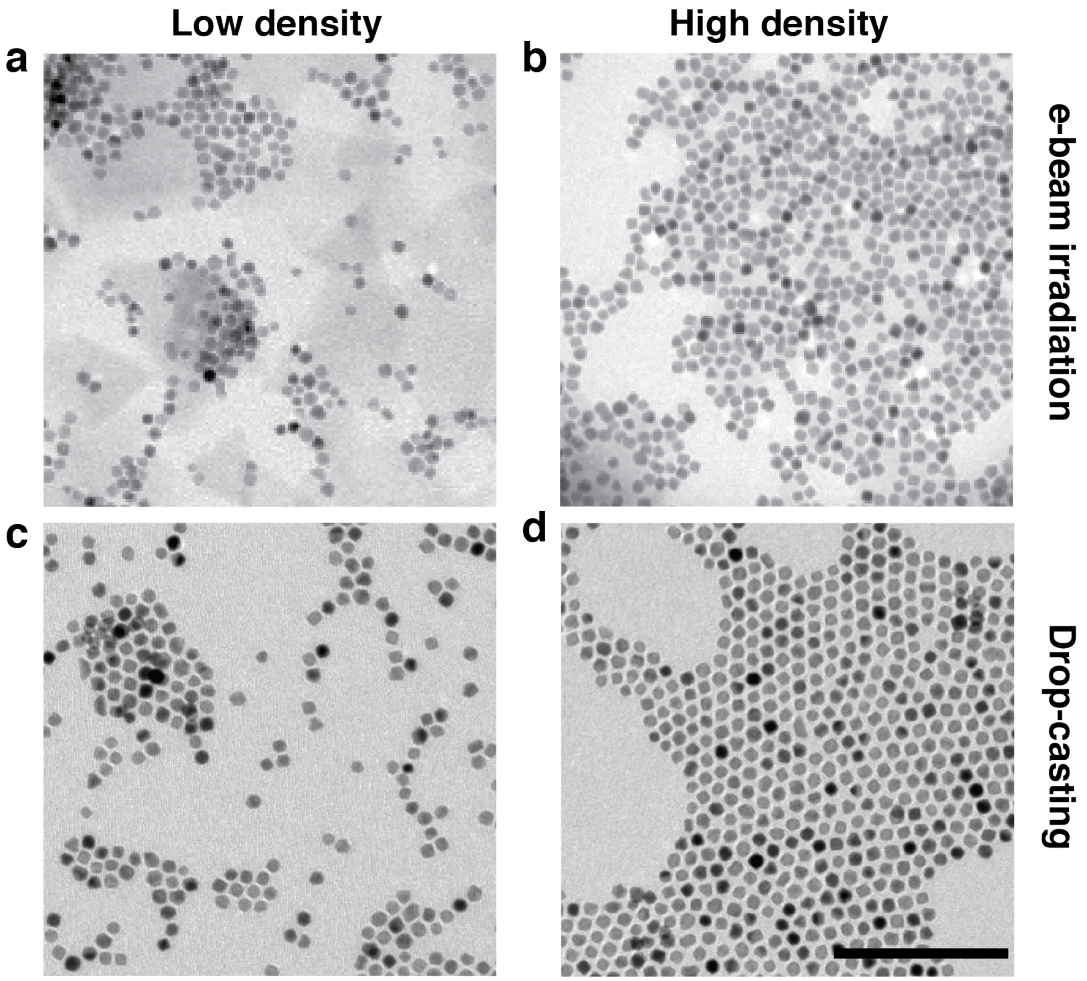

Figure 2.4. TEM images of NCs assembly formed under electron beam irradiation (panels **(a)** and **(b)**) and drop casting (panels **(c)** and **(d)**) on SiNx TEM grid. The scale bar is 100 nm.

In-situ liquid cell TEM observation is the only method we know of that can offer the types of trajectories shown here, so it is desirable to determine if there are other additional effects besides evaporation that the beam could have on the sample. Possible effects include mechanical momentum transfer, atomic displacement, bond breakage, heating, radiolysis, and charging amongst numerous others. We see no strong evidence that any of these processes alter the trajectories. We have calculated the beam induced heating and it is very small. We have calculated the degree of momentum transfer and it too is very small. It is more difficult to make any definitive statements regarding chemical changes induced by the beam. There is no question that the e-beam could be chemically perturbative, and it will require substantial more study to fully establish if this is happening.[106-108] The close similarity in the final structures between those observed here and those obtained by standard evaporation techniques shows that at least the e-beam does not change the final outcome of the assembly process.

2.5 Growth of Domains by Addition of Nanocrytals

In previous studies, convective transport of microparticles by capillary forces was found to be a main factor governing growth of domains as well as nucleation. In **Fig. 2.5** we show that this indeed is the case here as well. NCs first form small ordered domains. These domains then grow by the addition of individual NCs, where a freely moving NC, marked with an arrow, adds to an ordered array of NCs. The left column displays TEM images and the right column the corresponding images with a rainbow color overlay to clarify the solvent boundary and dried areas. The color scheme shows the white areas as low contrast regions due to drying of the solvent. Over the entire observation time NCs in the ordered array are blinking which indicates the rapid changes in their crystal orientation, demonstrating that they are still in wet conditions. The tagged NC approaches the array and fluctuates continuously upon contact until it fills the vacancy. While in ordinary nucleation theory the mobility of single particles is Brownian-like, in the present case, it seems to be coupled strongly with the drying vapor front.

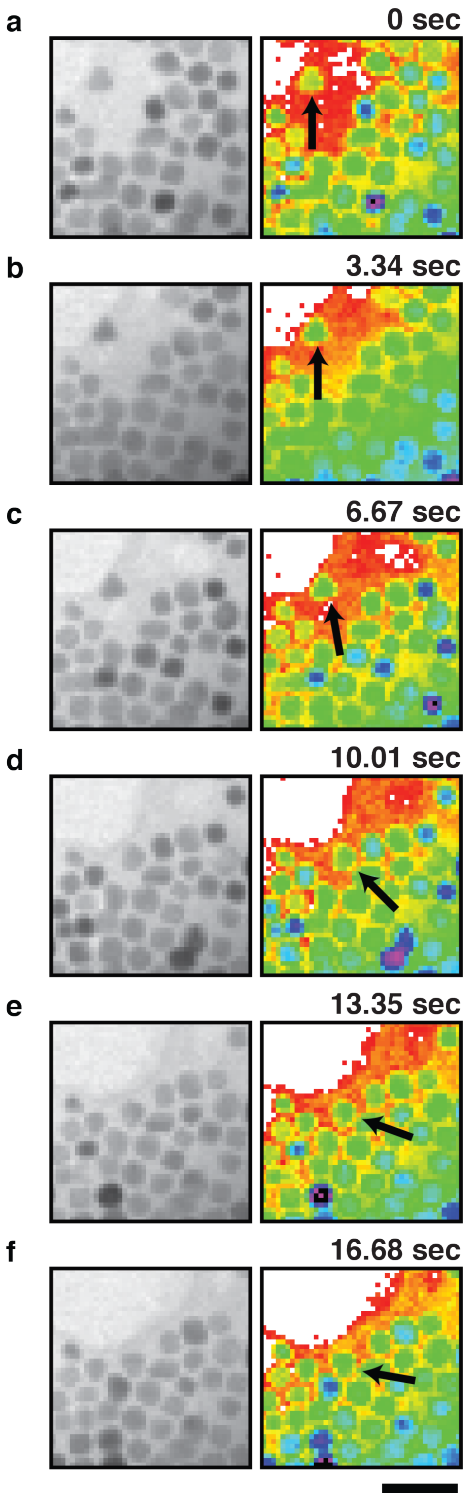

Figure 2.5. NC addition onto domain of superlattice. **(a)** – **(f)** Snapshots from Movie 3 at different times (left frames) and a corresponding color map with rainbow color scale (right frames). Contrast of rainbow color was calibrated such that white color corresponds to dried area. Arrow indicates a NC that moves laterally and rotates until it adequately fills in a vacancy in domain. The scale bar is 25 nm.

2.6 Single Particle Trajectories during Nanocrystal Self-Assembly

We find that individual NCs follow different pathways to their ordered positions in the final assembled domain. Trajectories of selected NCs from **Fig. 2.2b** and their MSD are shown in **Fig. 2.6a** and **2.6b**. Some NCs, labeled by scaled orange color, are continuously dragged by the solvent throughout the assembly formation in a small distance scale compared to the average MSD for the selected 51 NCs (green line). Other NCs, labeled by scaled blue color, follow a different pathway. They are dragged by the solvent at the beginning until they agglomerate into a sparse amorphous structure. Local fluctuations and further drying drives the NCs into their final ordered structure, as indicated by the decline in the slope of the MSD. Simulated trajectories in **Fig. 2.6c** also show that individual NCs dragged by the solvent front follow different pathways. Three NCs that show distinct dynamics are enlarged and marked in red, brown, and blue squares. The blue NC is carried across a large distance by the solvent front, while the other NCs cover a relatively small distance. In addition, depending on how the solvent front recedes, NCs that are close to each other at early times before assembly occurs (red and brown squares) can end at quite different locations in the assembled domain. The individual NC trajectories are not only affected by the capillary forces imposed by the solvent but also by local fluctuations that lead to distinct dynamics for individual NCs.

Changes of the local density of individual NCs contracted by strong solvent dragging (blue NCs in **Fig. 2.6a**) and NCs (orange NCs in **Fig. 2.6b**) dragged continuously are distinct while the formation superlattice: fluctuation with high local density and slow increase in small local density, respectively. **Figure 2.7** shows position change of these two groups of NCs at different times. Blue and red NCs are in random positions at the beginning of evaporation. However blue NCs gradually localize in the center of final assembled domain after dynamic overlapping with each other during strong dragging. Areal density of blue NCs reaches about 0.7 from relatively early stage (about 20 sec) and fluctuate throughout the time period due to the formation of amorphous agglomerates in **Fig. 2.8b**. Then, flattening at the later stage pushes them to 2D order as indicated by coincidence of areal density drop and increase of Ψ_6. The time for this abrupt increase of Ψ_6 of blue NCs matches with the moment when Ψ_6 of entire NCs show the same behavior (**Fig. 2.8a**). In contrary, both of areal density and Ψ_6 of red NCs gradually increase throughout entire time period (**Fig. 2.8c**). This implies that NCs positioning in the core of the fsinal ordered domain mainly contribute to the formation of amorphous agglomerates at the intermediate stage and boundary NCs are gradually contracted to domain.

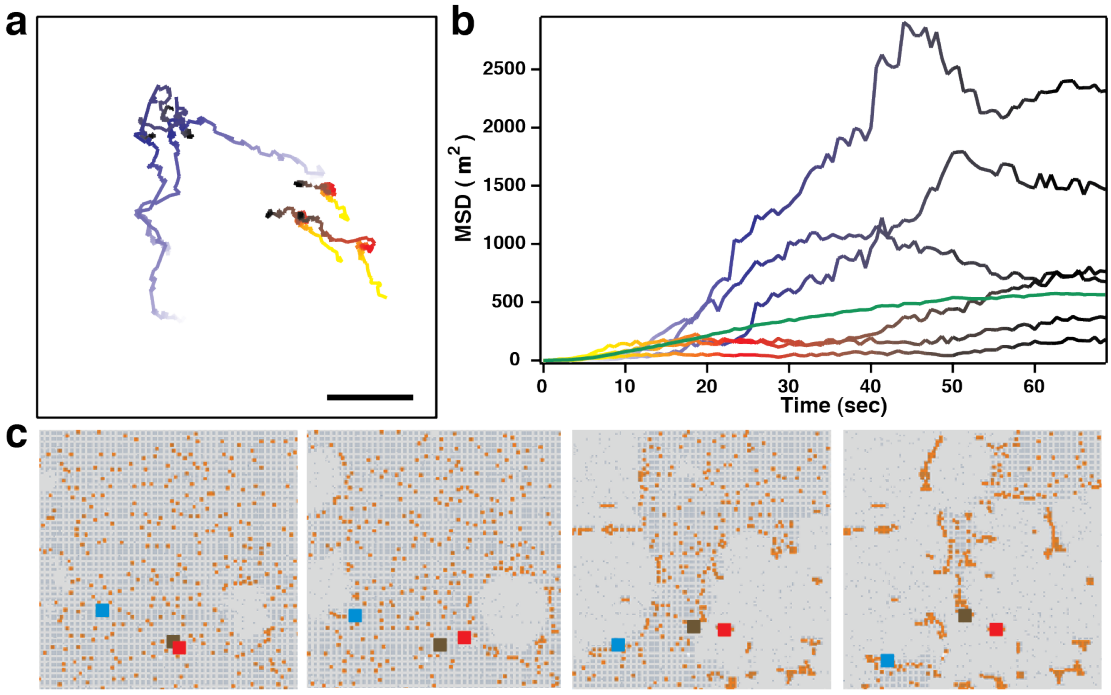

Figure 2.6. Individual NCs motion in liquid phase TEM observation and lattice gas modeling. **(a)** Trajectories of selected individual NCs from Fig. 1b for a time step of $\delta t = \frac{1}{3}$ sec. The time variable is labeled with blue and orange color scale for different types of trajectories. Black color indicates final stage of movement. The scale bar is 20 nm. **(b)** MSD of individual NCs shown in panel (a) with the same color scale along with the average MSD of the selected 51 NCs (green line). **(c)** Trajectories from lattice gas simulations. Selected NCs are enlarged and colored with red, brown, and blue to signify their motion. Time increases from left to right, for times (in MC steps) 1000, 1200, 1400, and 1600, respectively. Parameters are identical to those in Fig. 1 for a coverage of $\rho = 10\%$, chemical potential $\mu = -3\frac{1}{8}\varepsilon_\ell$, and temperature $T = 2\varepsilon_\ell$. Image size corresponds to approximately 50×50 nm^2.

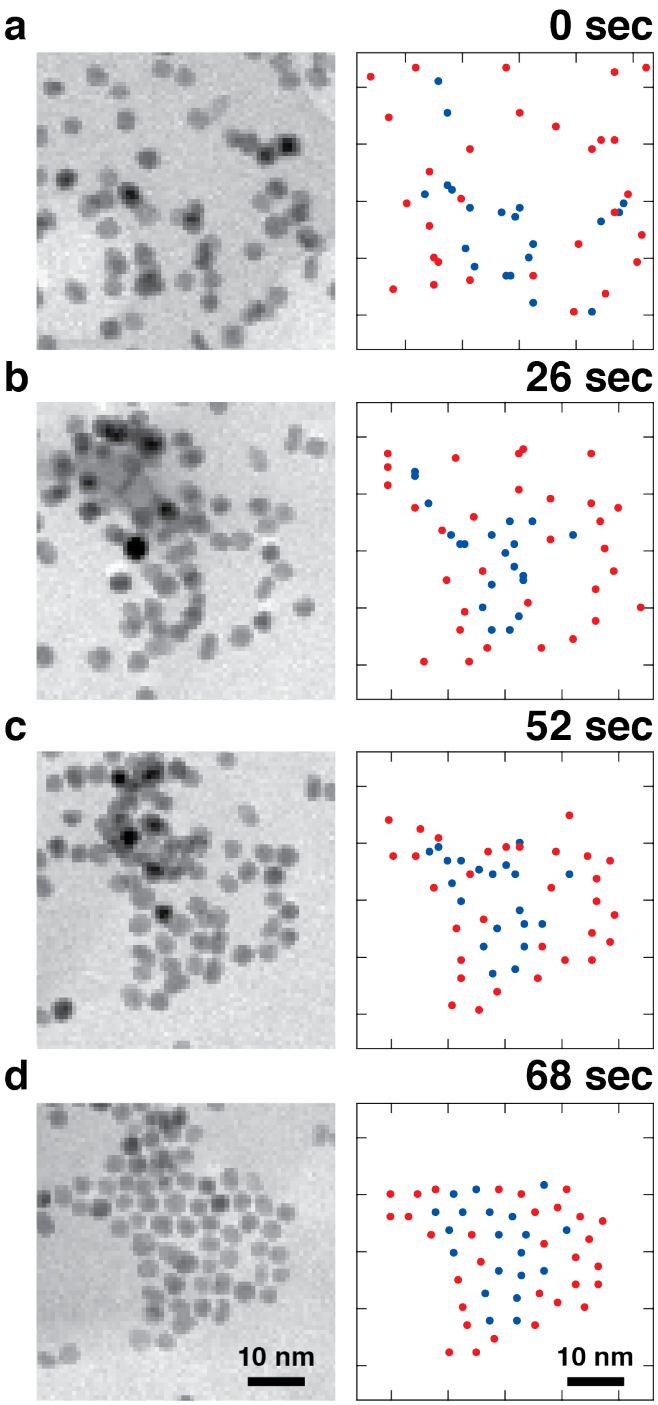

Figure 2.7. TEM images and color labeled positions at different times. NCs experiencing fluctuation of high local areal density in blue and NCs showing gradual increase of small local areal density in red.

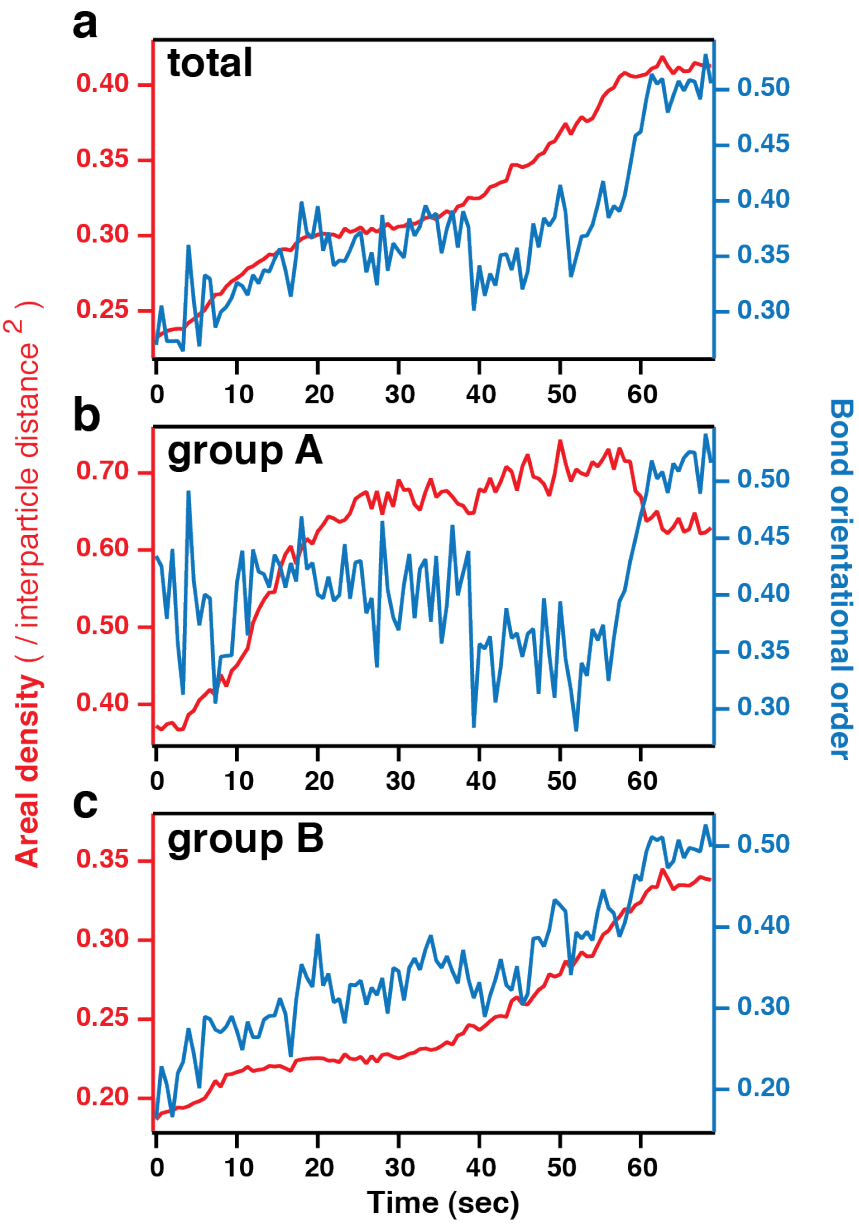

Figure 2.8. Areal density of NCs and the 2D bond orientational order parameter, a measure of crystalline ordering, as a function of time for **(a)** total NCs forming the final domain, **(b)** blue colored NCs, and **(c)** red colored NCs in **Fig. 2.7**.

2.7 Superlattice Formation from the NC Solution with Volume Fraction Change

NC trajectories and pathways for forming assembly are possibly subject to change in different volume fraction of NCs in solvent. We have studied two different volume fractions: low density and high density compared to the NC solution used in previous sections. Variation of volume fraction was achieved by diluting and concentrating the NC solution used for previous section with the same solution mixture (*o*-dichlorobenzne : oleylamine = 4 : 1 in volume) and the liquid cell sample preparation steps are identical.

Dispersed with low density in solvent, NCs first show large inter-NC distances before evaporation starts in **Fig. 2.9a**. In this case, solvent drags NCs while evaporation boundary proceeds as we saw in previous situation, thus, solvent performs the main driving force to move NCs in this concentration limit as well. Differently from the high concentration case, here, NCs do not undergo amorphous agglomerates as an intermediate stage of assembly. NCs are gradually dragged from the sparse locations at the beginning to the final small domains in **Fig. 2.9a**. **Figure 2.9b**, areal density and 2D bond orientational order plot as a function of time, also reflect this behavior. Both plots exhibit monotonous increases which imply that the orderness of assembled domains is formed steadily as solvent evaporation converges NCs.

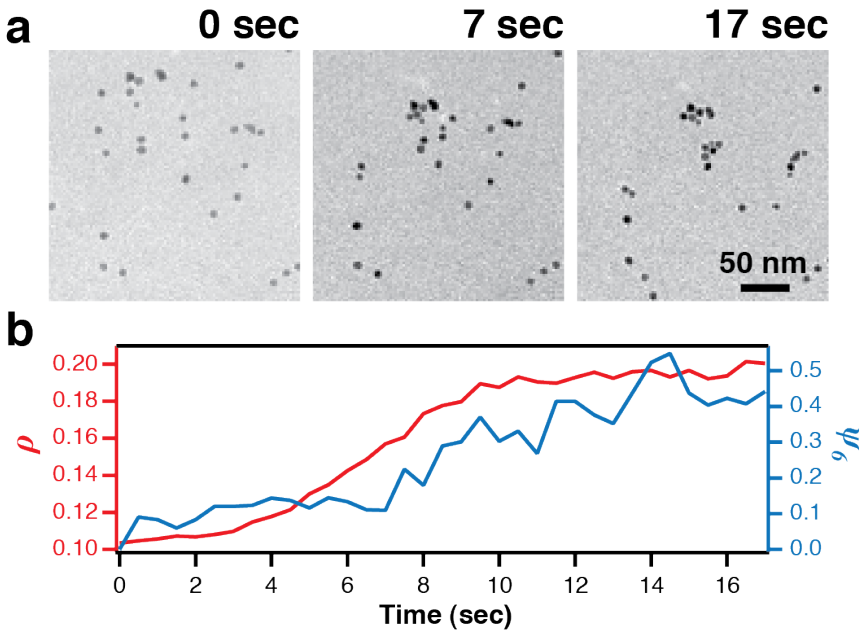

Figure 2.9. Superlattice formation of NCs in the solution of low volume fraction. **(a)** TEM still-snapshots at different times. **(b)** Areal density of NCs and the 2D bond orientational order parameter, a measure of crystalline ordering, as a function of time.

We also investigated self-assembly formation from NC solution with high volume fraction. **Figure 2.10** summarizes TEM still snap-shots from real time movie of superlattice formation, corresponding Delauney triangulations which indicates nearest neighboring NC network, and radial-distribution function from the beginning of our observation. Our observation begins with a large fraction of amorphous agglomerates of NCs. We assume they are already formed during the evaporation of excess *o*-dichlorobenzenen of liquid cell preparation before we start imaging. We also tracked 2D projected positions of NCs in different times and used them for Delauney triangulations and radial-distribution functions. Overlapping NCs in several monolayer thickness within amorphous agglomerates results in non-homogeneous triangles in Delauney triangulations. Noisy peak in radial-distribution function with the smaller distance than inter-NC distance of final assembled superlattice also proves the existence of agglomerates. These agglomerates are pushed onto substrate as the solvent evaporates as indicated in homogeneous triangles and a strong peak in radial-distribution function at the inter-NC distance. During this process, NCs not only form 2D array but also evolves orderness. Bond orientation order increases from 0.3595 to 0.4327 while the areal density decreases from 0.4765 to 0.4092 (inter-NC distance^2). This behavior is actually similar to what we have observed in **Fig. 2.2** and **2.3** of an intermediate volume fraction of NCs.

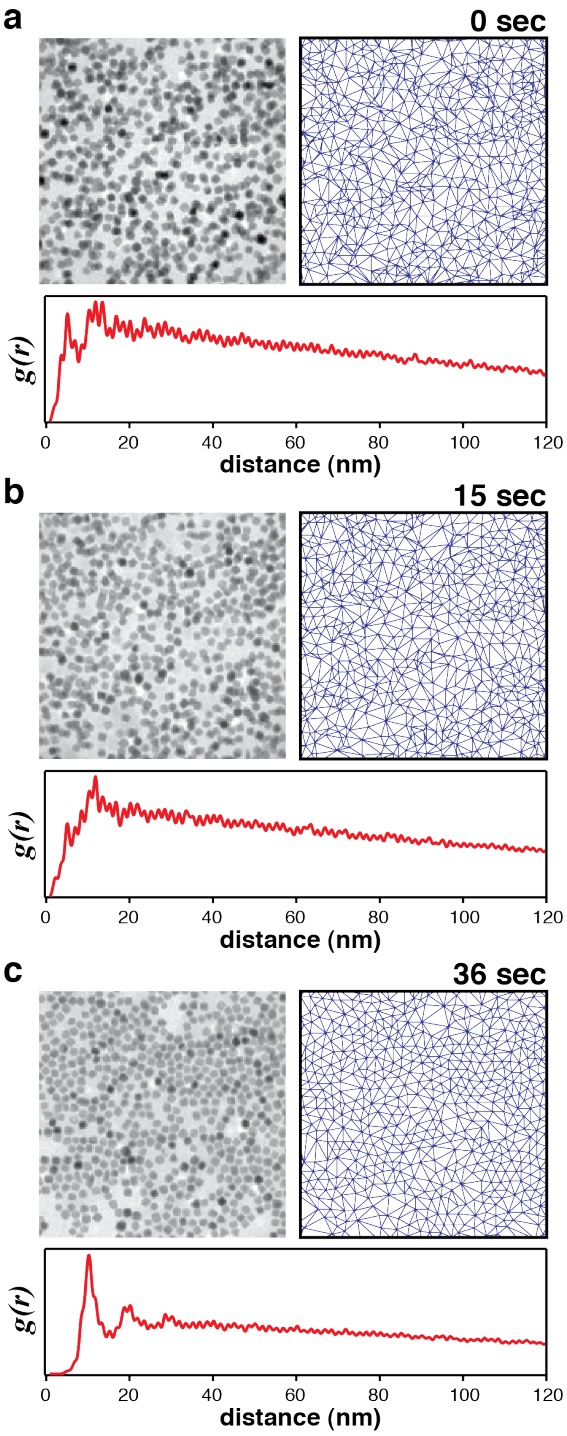

Figure 2.10. Superlattice formation of NCs in the solution of high volume fraction. TEM still-snapshots at different times together with the corresponding Delauney triangulations, (nearest neighbor network) and radial-distribution functions at different times. Areal density and bond orientational order for three different times are 0.4765, 0.3595 (0 sec), 0.4584, 0.3703 (15 sec), and 0.4092, 0.4327 (36 sec). Densities are in (inter-NC distance)^2.

Consequently, dragging of NCs induced by the solvent evaporation performs the major role for superlattice formation throughout the range of NC volume fraction in solvent. This picture is also sustained in coarse-grained lattice gas modeling. In any volume fraction from 10 % to 50 %, NCs eventually form well-ordered superlattice with a corresponding coverage in a low diffusive limit of NCs (**Fig. 2.11**). However, the effect of dragging by solvent fluctuation results in different mechanism of superlattice formation in volume fraction range. At the low volume fraction, solvent steadily drags NCs until they form ordered small domains. Contrary to this, NCs undergo amorphous agglomerates as an intermediate stage, presumably, when the initial volume fraction is larger than a critical value.

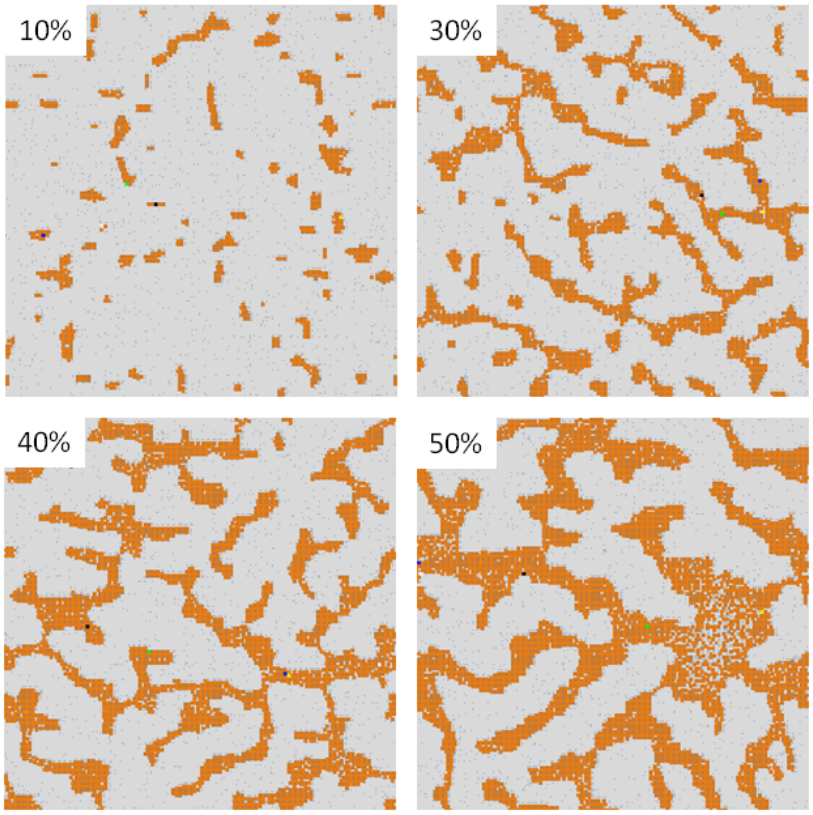

Figure 2.11. Simulated superlattice patterns with varying coverage of NCs under low NC diffusivity. Parameters are identical to those in Fig. 1 with $\mu = -3\frac{1}{4}\varepsilon_\ell$ and $T = 2\varepsilon_\ell$.

Chapter 3.

Concluding Remarks

Direct observation of colloidal NC dynamics enables us to understand mechanisms behind the growth and their dynamic behavior in a medium, a liquid. Moreover, we are able to track dynamics in a single NC level and compare our observation with their ensemble behavior which is usually obtained from other analytical tools. *In-situ* observation probably guide to the rational design of functional nanomaterials and their applications.

In chapter 1, we introduce the GLC as a new type of liquid cell advancing the imaging of liquid-phase systems; encapsulated liquid specimens are observed with an electron microscope at the highest resolution possible to date with minimal sample perturbation. The GLC has enabled the study of colloidal nanocrystal growth with unprecedented resolution revealing a host of previously unexpected phenomena. We have directly observed the steps of nanocrystal coalescence and oriented attachment at an atomic level. The GLC can be readily applied to directly study a diversity of fluid-phase samples which beg detailed observation.

In chapter 2, we used a liquid phase TEM to image the drying-mediated self-assembly of NCs in real time. As the solvent evaporates under electron beam irradiation, NCs are dragged by the receding solvent front to form an ordered superlattice array. The superlattice formation is composed of several steps and actual crystallization takes place after the NCs are contracted into a dense disordered phase. In addition, domains can continue to grow by the addition of NCs that are dragged by capillary forces. Lattice gas simulation results provide a consistent picture when the motion of NCs is governed by solvent fluctuations and capillary forces rather than Brownian motion. Our work provides experimental tools needed to better understand the mechanisms of drying-mediated self-assembly at the level of single NC dynamics.

References

1. Eswaramoorthy, S.K., Howe, J.M. & Muralidharan, G. In situ determination of the nanoscale chemistry and behavior of solid-liquid systems. *Science* **318**, 1437-40 (2007).

2. Radmilovic, V. *et al.* Highly monodisperse core-shell particles created by solid-state reactions. *Nature materials* **10**, 710-5 (2011).

3. Wen, C.-Y. *et al.* Formation of compositionally abrupt axial heterojunctions in silicon-germanium nanowires. *Science* **326**, 1247-50 (2009).

4. Zewail, A.H. Four-dimensional electron microscopy. *Science* **328**, 187-93 (2010).

5. Williamson, M.J., Tromp, R.M., Vereecken, P.M., Hull, R. & Ross, F.M. Dynamic microscopy of nanoscale cluster growth at the solid-liquid interface. *Nature materials* **2**, 532-6 (2003).

6. de Jonge, N. & Ross, F.M. Electron microscopy of specimens in liquid. *Nature nanotechnology* **6**, 695-704 (2011).

7. Evans, J.E., Jungjohann, K.L., Browning, N.D. & Arslan, I. Controlled growth of nanoparticles from solution with in situ liquid transmission electron microscopy. *Nano letters* **11**, 2809-13 (2011).

8. Liu, K.-L. *et al.* Novel microchip for in situ TEM imaging of living organisms and bio-reactions in aqueous conditions. *Lab on a chip* **8**, 1915-21 (2008).

9. Zheng, H., Claridge, S. a, Minor, A.M., Alivisatos, a P. & Dahmen, U. Nanocrystal diffusion in a liquid thin film observed by in situ transmission electron microscopy. *Nano letters* **9**, 2460-5 (2009).

10. Zheng, H. *et al.* Observation of single colloidal platinum nanocrystal growth trajectories. *Science* **324**, 1309-12 (2009).

11. Erni, R. *et al.* Stability and dynamics of small molecules trapped on graphene. *Physical Review B* **82**, 1-6 (2010).

12. Kolmakov, A. *et al.* Graphene oxide windows for in situ environmental cell photoelectron spectroscopy. *Nature nanotechnology* **6**, 651-7 (2011).

13. Lee, Z., Jeon, K., Dato, A., Erni, R. & Richardson, T. Direct Imaging of Soft−Hard Interfaces Enabled by Graphene. *Nano letters* **9**, 1-5 (2009).

14. Meyer, J.C., Girit, C.O., Crommie, M.F. & Zettl, a Imaging and dynamics of light atoms and molecules on graphene. *Nature* **454**, 319-22 (2008).

15. Nair, R.R. *et al.* Graphene as a transparent conductive support for studying biological molecules by transmission electron microscopy. *Applied Physics Letters* **97**, 153102 (2010).

16. Novoselov, K.S. *et al.* Two-dimensional atomic crystals. *Proceedings of the National Academy of Sciences of the United States of America* **102**, 10451-3 (2005).

17. Wu, Y. a *et al.* Utilizing boron nitride sheets as thin supports for high resolution imaging of nanocrystals. *Nanotechnology* **22**, 195603 (2011).

18. Koenig, S.P., Boddeti, N.G., Dunn, M.L. & Bunch, J.S. Ultrastrong adhesion of graphene membranes. *Nature nanotechnology* **6**, 543-6 (2011).

19. Mohanty, N., Fahrenholtz, M., Nagaraja, A., Boyle, D. & Berry, V. Impermeable graphenic encasement of bacteria. *Nano letters* **11**, 1270-5 (2011).

20. Xu, K., Cao, P. & Heath, J.R. Graphene visualizes the first water adlayers on mica at ambient conditions. *Science* **329**, 1188-91 (2010).

21. Yuk, J.M. *et al.* Graphene veils and sandwiches. *Nano letters* **11**, 3290-4 (2011).

22. Li, X. *et al.* Highly conducting graphene sheets and Langmuir-Blodgett films. *Nature nanotechnology* **3**, 538-42 (2008).

23. Li, X. *et al.* Large-area synthesis of high-quality and uniform graphene films on copper foils. *Science* **324**, 1312-4 (2009).

24. Regan, W. *et al.* A direct transfer of layer-area graphene. *Applied Physics Letters* **96**, 113102 (2010).

25. Xie, X. *et al.* Controlled Fabrication of High-Quality Carbon Nanoscrolls from Monolayer Graphene. *Nano letters* **9**, 2565-70 (2009).

26. Lim, T., McCarthy, D., Hendy, S. & Stevens, K. Real-Time TEM and Kinetic Monte Carlo Studies of the Coalescence of Decahedral Gold Nanoparticles. *ACS nano* **3**, 3809-3813 (2009).

27. Palasantzas, G., Vystavel, T., Koch, S. a. & De Hosson, J.T.M. Coalescence aspects of cobalt nanoparticles during in situ high-temperature annealing. *Journal of Applied Physics* **99**, 024307 (2006).

28. Chiu, C.-Y. *et al.* Platinum nanocrystals selectively shaped using facet-specific peptide sequences. *Nature chemistry* **3**, 393-9 (2011).

29. Lu, X., Rycenga, M., Skrabalak, S.E., Wiley, B. & Xia, Y. Chemical synthesis of novel plasmonic nanoparticles. *Annual review of physical chemistry* **60**, 167-92 (2009).

30. Fang, Z.Z. & Wang, H. Densification and grain growth during sintering of nanosized particles. *International Materials Reviews* **53**, 326-352 (2008).

31. Baker, J.L., Widmer-Cooper, A., Toney, M.F., Geissler, P.L. & Alivisatos, a P. Device-scale perpendicular alignment of colloidal nanorods. *Nano letters* **10**, 195-201 (2010).

32. Baranov, D. *et al.* Assembly of colloidal semiconductor nanorods in solution by depletion attraction. *Nano letters* **10**, 743-9 (2010).

33. Lin, X., Jaeger, H. & Sorensen, C. Formation of long-range-ordered nanocrystal superlattices on silicon nitride substrates. *The journal of physical chemistry. B* **105**, 3353-3357 (2001).

34. Mueggenburg, K.E., Lin, X.-M., Goldsmith, R.H. & Jaeger, H.M. Elastic membranes of close-packed nanoparticle arrays. *Nature materials* **6**, 656-60 (2007).

35. Brown, L.O. & Hutchison, J.E. Formation and Electron Diffraction Studies of Ordered 2-D and 3-D Superlattices of. *The journal of physical chemistry. B* **105**, 8911-8916 (2001).

36. Grzelczak, M., Vermant, J., Furst, E.M. & Liz-Marzán, L.M. Directed self-assembly of nanoparticles. *ACS nano* **4**, 3591-605 (2010).

37. Guerrero-Martínez, A., Pérez-Juste, J., Carbó-Argibay, E., Tardajos, G. & Liz-Marzán, L.M. Gemini-surfactant-directed self-assembly of monodisperse gold nanorods into standing superlattices. *Angewandte Chemie (International ed. in English)* **48**, 9484-8 (2009).

38. He, S. *et al.* Formation of silver nanoparticles and self-assembled two-dimensional ordered superlattice. *Langmuir* **17**, 1571-1575 (2001).

39. Kolny, J., Kornowski, A. & Weller, H. Self-Organization of Cadmium Sulfide and Gold Nanoparticles by Electrostatic Interaction. *Nano Letters* **2**, 361-364 (2002).

40. Korgel, B. & Fitzmaurice, D. Condensation of ordered nanocrystal thin films. *Physical review letters* **1**, 3531-3534 (1998).

41. Korgel, B., Fullam, S. & Connolly, S. Assembly and Self-Organization of Silver Nanocrystal Superlattices : Ordered " Soft Spheres ."*The journal of physical chemistry. B* **102**, 8379-8388 (1998).

42. Li, F., Josephson, D.P. & Stein, A. Colloidal assembly: the road from particles to colloidal molecules and crystals. *Angewandte Chemie (International ed. in English)* **50**, 360-88 (2011).

43. Luedtke, W. Structure, dynamics, and thermodynamics of passivated gold nanocrystallites and their assemblies. *The Journal of Physical Chemistry* **100**, 13323-9 (1996).

44. Pietrobon, B. & McEachran, M. Synthesis of size-controlled faceted pentagonal silver nanorods with tunable plasmonic properties and self-assembly of these nanorods. *ACS nano* **3**, 21-26 (2008).

45. Prasad, B.L.V., Sorensen, C.M. & Klabunde, K.J. Gold nanoparticle superlattices. *Chemical Society reviews* **37**, 1871-83 (2008).

46. Redl, F.X., Cho, K.-S., Murray, C.B. & O'Brien, S. Three-dimensional binary superlattices of magnetic nanocrystals and semiconductor quantum dots. *Nature* **423**, 968-71 (2003).

47. Shevchenko, E.V., Talapin, D.V., Kotov, N. a, O'Brien, S. & Murray, C.B. Structural diversity in binary nanoparticle superlattices. *Nature* **439**, 55-9 (2006).

48. Shevchenko, E.V., Talapin, D.V., Murray, C.B. & O'Brien, S. Structural characterization of self-assembled multifunctional binary nanoparticle superlattices. *Journal of the American Chemical Society* **128**, 3620-37 (2006).

49. Stoeva, S., Prasad, B. & Uma, S. Face-centered cubic and hexagonal closed-packed nanocrystal superlattices of gold nanoparticles prepared by different methods. *The journal of physical chemistry. B* **107**, 7441-7448 (2003).

50. Talapin, D.V. *et al.* Quasicrystalline order in self-assembled binary nanoparticle superlattices. *Nature* **461**, 964-967 (2009).

51. Urban, J.J., Talapin, D.V., Shevchenko, E.V. & Murray, C.B. Self-assembly of PbTe quantum dots into nanocrystal superlattices and glassy films. *Journal of the American Chemical Society* **128**, 3248-55 (2006).

52. Ackerson, B. Classical growth of hard-sphere colloidal crystals. *Physical Review E* **52**, 6448-60 (1995).

53. Anderson, V. Insights into Phase Transition Kinetics from Colloid Science. *Nature* **416**, 811-815 (2002).

54. Cleveland, C.L. & Landman, U. Dynamics of cluster-surface collisions. *Science* **257**, 355-361 (1992).

55. Kalsin, A.M. *et al.* Electrostatic self-assembly of binary nanoparticle crystals with a diamond-like lattice. *Science* **312**, 420-4 (2006).

56. Whitesides, G.M. & Grzybowski, B. Self-assembly at all scales. *Science* **295**, 2418-21 (2002).

57. Bishop, K.J.M., Wilmer, C.E., Soh, S. & Grzybowski, B. a Nanoscale forces and their uses in self-assembly. *Small* **5**, 1600-30 (2009).

58. Tang, J. & Ge, G. Gas-liquid-solid phase transition model for two-dimensional nanocrystal self-assembly on graphite. *The Journal of Physical Chemistry B* **106**, 5653-5658 (2002).

59. Schapotschnikow, P. & Pool, R. Molecular Simulations of Interacting Nanocrystals. *Nano letters* **8**, 2930-4 (2008).

60. Kletenik-Edelman, O. & Ploshnik, E. Drying-Mediated Hierarchical Self-Assembly of Nanoparticles: A Dynamical Coarse-Grained Approach. *The Journal of Physical Chemistry. C* **112**, 4498-4506 (2008).

61. Kletenik-Edelman, O., Sztrum-Vartash, C.G. & Rabani, E. Coarse-grained lattice models for drying-mediated self-assembly of nanoparticles. *Journal of Materials Chemistry* **19**, 2872-6 (2009).

62. Rabani, E., Reichman, D. & Geissler, P. Drying-mediated self-assembly of nanoparticles. *Nature* **426**, 271-4 (2003).

63. Deegan, R.D., Bakajin, O. & Dupont, T.F. Capillary flow as the cause of ring stains from dried liquid drops. *Nature* **389**, 827-9 (1997).

64. Kralchevsky, P. a & Nagayama, K. Capillary interactions between particles bound to interfaces, liquid films and biomembranes. *Advances in colloid and interface science* **85**, 145-92 (2000).

65. Kralchevsky, P. a. & Denkov, N.D. Capillary forces and structuring in layers of colloid particles. *Current Opinion in Colloid & Interface Science* **6**, 383-401 (2001).

66. Luedtke, W. Slip diffusion and Levy flights of an adsorbed gold nanocluster. *Physical review letters* **82**, 3835-3838 (1999).

67. Auer, S. & Frenkel, D. Prediction of absolute crystal-nucleation rate in hard-sphere colloids. *Nature* **409**, 1020-3 (2001).

68. Blaaderen, A.V. Real-space structure of colloidal hard-sphere glasses. *Science* **270**, 1177-9 (1995).

69. Crocker, J. & Grier, D. Methods of Digital Video Microscopy for Colloidal Studies. *Journal of Colloid and Interface Science* **310**, 298-310 (1996).

70. de Hoog, E., Kegel, W., van Blaaderen, a. & Lekkerkerker, H. Direct observation of crystallization and aggregation in a phase-separating colloid-polymer suspension. *Physical Review E* **64**, 1-9 (2001).

71. Denkov, N., Velev, O., Kralchevski, P. & Ivanov, I. Mechanism of formation of two-dimensional crystals from latex particles on substrates. *Langmuir* **8**, 3183-3190 (1992).

72. Dimitrov, A.S. & Nagayama, K. Continuous Convective Assembling of Fine Particles into Two-Dimensional Arrays on Solid Surfaces. *Langmuir* **12**, 1303-11 (1996).

73. Gasser, U., Weeks, E.R., Schofield, A., Pusey, P.N. & Weitz, D. a Real-space imaging of nucleation and growth in colloidal crystallization. *Science* **292**, 258-62 (2001).

74. Grier, D. The microscopic dynamics of freezing in supercooled colloidal fluids. *The Journal of chemical physics* **100**, 9088-9095 (1994).

75. Habdas, P. Video microscopy of colloidal suspensions and colloidal crystals. *Current opinion in colloid & interface science* **7**, 196-203 (2002).

76. Kegel, W.K. Direct Observation of Dynamical Heterogeneities in Colloidal Hard-Sphere Suspensions. *Science* **287**, 290-293 (2000).

77. Moore, L.J., Dear, R.D., Summers, M.D., Dullens, R.P. a & Ritchie, G. a D. Direct observation of grain rotation-induced grain coalescence in two-dimensional colloidal crystals. *Nano letters* **10**, 4266-72 (2010).

78. Murray, C. a., Van winkleD. H. & Wenk, R. a. Digital imaging studies of submicron colloidal spheres confined into a single layer between two smooth glass plates: Two dimensional melting. *Phase Transitions* **21**, 93-126 (1990).

79. Murray, C. a. & Grier, D.G. Video Microscopy of Monodisperse Colloidal Systems. *Annual Review of Physical Chemistry* **47**, 421-462 (1996).

80. Ramos, L. Surfactant-Mediated Two-Dimensional Crystallization of Colloidal Crystals. *Science* **286**, 2325-2328 (1999).

81. Abécassis, B., Testard, F. & Spalla, O. Gold Nanoparticle Superlattice Crystallization Probed In Situ. *Physical Review Letters* **100**, 1-4 (2008).

82. Bigioni, T.P. *et al.* Kinetically driven self assembly of highly ordered nanoparticle monolayers. *Nature materials* **5**, 265-270 (2006).

83. Connolly, S., Fullam, S. & Korgel, B. Time-resolved small-angle X-ray scattering studies of nanocrystal superlattice self-assembly. *Journal of the American Chemical Society* **7863**, 2969-70 (1998).

84. Ge, G. & Brus, L.E. Fast Surface Diffusion of Large Disk-Shaped Nanocrystal Aggregates. *Nano Letters* **1**, 219-222 (2001).

85. Jiang, Z., Lin, X.-M., Sprung, M., Narayanan, S. & Wang, J. Capturing the crystalline phase of two-dimensional nanocrystal superlattices in action. *Nano letters* **10**, 799-803 (2010).

86. Lee, B. *et al.* Comparison of structural behavior of nanocrystals in randomly packed films and long-range ordered superlattices by time-resolved small angle X-ray scattering. *Journal of the American Chemical Society* **131**, 16386-8 (2009).

87. Narayanan, S., Wang, J. & Lin, X.-M. Dynamical Self-Assembly of Nanocrystal Superlattices during Colloidal Droplet Evaporation by in situ Small Angle X-Ray Scattering. *Physical Review Letters* **93**, 1-4 (2004).

88. Savage, J., Blair, D., Levine, A. & Guyer, R. Imaging the sublimation dynamics of colloidal crystallites. *Science* **314**, 795-8 (2006).

89. Ohara, P. & Heath, J. Self-Assembly of Submicrometer Rings of Particles from Solutions of Nanoparticles. *Angewandte Chemie (International ed. in English)* **36**, 1077-1080 (1997).

90. Tsung, C.-K. *et al.* Sub-10 nm platinum nanocrystals with size and shape control: catalytic study for ethylene and pyrrole hydrogenation. *Journal of the American Chemical Society* **131**, 5816-22 (2009).

91. Lee, H. *et al.* Morphological control of catalytically active platinum nanocrystals. *Angewandte Chemie (International ed. in English)* **45**, 7824-8 (2006).

92. Sztrum, C. G. & Rabani, E. Out-of-Equilibrium Self-Assembly of Binary Mixtures of Nanoparticles. *Advanced Materials* **18**, 565-571 (2006).

93. Sztrum, C.G., Hod, O. & Rabani, E. Self-assembly of nanoparticles in three-dimensions: formation of stalagmites. *The journal of physical chemistry. B* **109**, 6741-7 (2005).

94. Yosef, G. & Rabani, E. Self-assembly of nanoparticles into rings: a lattice-gas model. *The journal of physical chemistry. B* **110**, 20965-72 (2006).

95. Ajaev, V. Evolution of dry patches in evaporating liquid films. *Physical Review E* **72**, 1-7 (2005).

96. Elbaum, M. how does a thin wetted film dry up? *Physical review letters* **72**, 3562-5 (1994).

97. Jaqaman, K., Loerke, D., Mettlen, M. & Kuwata, H. Robust single-particle tracking in live-cell time-lapse sequences. *Nature methods* **5**, 695-702 (2008).

98. Yang, H. Progress in single-molecule spectroscopy in cells. *Current opinion in chemical biology* **14**, 3-9 (2010).

99. Montiel, D. & Yang, H. Real-time three-dimensional single-particle tracking spectroscopy for complex systems. *Laser & Photonics Reviews* **4**, 374-385 (2010).

100. van Honschoten, J.W., Brunets, N. & Tas, N.R. Capillarity at the nanoscale. *Chemical Society reviews* **39**, 1096-114 (2010).

101. Reinhard, B.M., Sheikholeslami, S., Mastroianni, A., Alivisatos, a P. & Liphardt, J. Use of plasmon coupling to reveal the dynamics of DNA bending and cleavage by single EcoRV restriction enzymes. *Proceedings of the National Academy of Sciences of the United States of America* **104**, 2667-72 (2007).

102. Rabideau, B.D., Pell, L.E., Bonnecaze, R.T. & Korgel, B. a Observation of long-range orientational order in monolayers of polydisperse colloids. *Langmuir* **23**, 1270-4 (2007).

103. Wang, Z., Alsayed, A.M., Yodh, A.G. & Han, Y. Two-dimensional freezing criteria for crystallizing colloidal monolayers. *The Journal of chemical physics* **132**, 154501 (2010).

104. Steinhardt, P. & Nelson, D. Bond orientational order in liquids and glasses. *Physical Review B* **28**, 784-805 (1983).

105. Savage, J. & Dinsmore, a. Experimental Evidence for Two-Step Nucleation in Colloidal Crystallization. *Physical Review Letters* **102**, 15-18 (2009).

106. Egerton, R.F., Li, P. & Malac, M. Radiation damage in the TEM and SEM. *Micron* **35**, 399-409 (2004).

107. Egerton, R.F., Wang, F. & Crozier, P. a Beam-induced damage to thin specimens in an intense electron probe. *Microscopy and microanalysis* **12**, 65-71 (2006).

108. Glaeser, R.M. Retrospective: radiation damage and its associated “information limitations”. *Journal of structural biology* **163**, 271-6 (2008).

Appendix

A1. Supporting Information for High-Resolution Observation of Colloidal Nanocrystal Growth Mechanisms using Graphene Liquid Cells

A1.1. Methods

Preparation of GLC sample. Growth dynamics of platinum NCs in a graphene liquid cell was observed *in-situ* using a TEAM I. A growth solution of Pt(acetylacetonate)$_2$ (10 mg/mL) in a mixture of *o*-dichlorobenzene and oleylamine (9:1 in volume ratio) was used. The success rate in producing viable GLCs is >90%.

Pt growth in GLC. The growth of platinum NCs was initiated by electron beam irradiation. Electron beam intensity was optimized onto local spots for the initial ~ 5 seconds of movies to capture the initial stage of NC growth. Initial liquid films were thin enough to capture these initial stages. The electron beam intensity was maintained same throughout observation time and provided optimal contrast for NC motions. With thicker liquid films, contrast is very poor; however, liquid thickness can also be thinned by very strong electron beam irradiation (such conditions did not apply to the data shown here). Our TEM observations reveals that graphene secure liquid within pockets throughout the duration of the recording, usually ten to twenty minutes. ”

Microscopy. The low magnification TEM imaging was performed in a JEM-2010 LaB_6 instrument (JEOL Ltd.) at 100 kV.

High-resolution TEM images were acquired with the TEAM 1 operated at 80kV at the National Center for Electron Microscopy. This electron microscope has a high-brightness gun (X-FEG) and probe as well as image and chromatic aberration correctors. The image corrector (C_s) was fine tuned to obtain a third-order spherical aberration of −10μm, which in consideration of the positive fifth-order aberration (C_5) of 2.5 mm yielded optimal phase contrast with slight positive defocus. The theoretical information limit of 0.05 nm can thus be achieved at 80 kV. The resulting electron dose is approximately 4×10^5 e^-/sec·nm^2. We set 0.03 seconds of exposure time, 0.23 seconds of read out time, and therefore 0.26 seconds of entire frame time to acquire time-serial images. More details of the microscope configuration can be found elsewhere [S1].

AFM images were taken on a MFP-3D scanning probe microscope (Asylum Research instruments). AFM imaging was performed on suspended GLC samples on Quantifoil TEM grids in non-contact mode using a V-shaped ‘NSC35’ probe C (phosphorus-doped Si with frequency f_c = 150 kHz, spring constants k = 4.5 N m^{-1}, and nominal tip radius 10 nm). All images were collected under ambient conditions at 23 °C with a scanning rate of 2.5-10 um/s.

SEM images were performed using FEI XL3000 at 5 kV.

Spectroscopy. The Raman measurements were performed using Renishaw inVia Raman microscope with 514 nm Ar ion laser.

A1.2. Text

Coalescence of Pt NCs. We observed twenty coalescence events between NCs with diameters greater than 1 nm. We assume that coalescence events of NCs with smaller size or parallel to the electron beam cannot be distinguished or detected, respectively, and thus are not considered. One important factor to consider prior to discussing coalescence dynamics is NCs rotational degree of freedom. **Figure A1.5** exhibits different lattice planes of a freely rotating NC at different times of observation. For this specific NC, lattice planes were observed eight times while the zone axis aligned with the beam over the course of the video; otherwise no fringes were observed off the crystal zone axes. Most coalescence we distinguished by lattice planes occur along the along {111} planes of either one or both NCs, as represented in **Fig. 1.6**, **Fig. A1.6**, and **Fig. A1.7**. Only two coalescence events surveyed merged on different planes of the contacting NCs: {110} plane for one and off-zone axis for the other (**Fig. A1.8**).

The ratios of two NC diameters in **Fig. 1.6b** and **1.6c** before coalescence are 0.75 and 0.71, respectively, which are similar with diameter ratios of two domains with twin boundaries after coalescence, 0.74 and 0.68 in **Fig. 1.6b** and **1.6c**, respectively. Diameter is calculated using $D=2(A/\pi)^{0.5}$, where A is the projected 2D area of the NC in the video images. This consistency of diameter ratio before and after coalescence is shown in all of NCs with twin boundaries.

A1.3. Supporting Figures and Legends

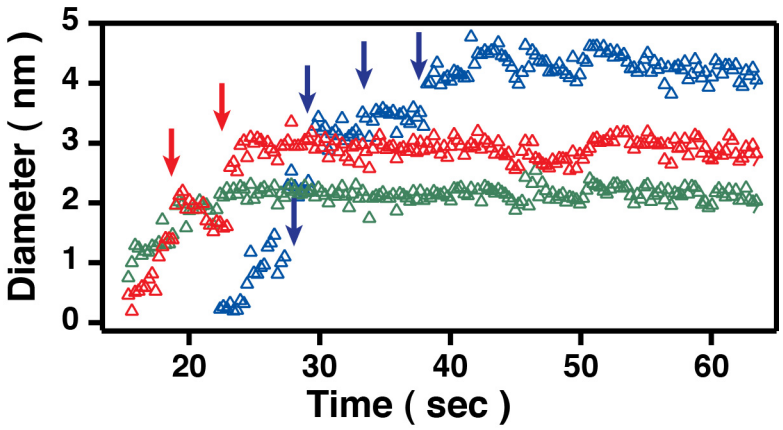

Figure A1.1. Growth trajectories of individual Pt NC in several pathways: gradual growth by monomer addition, green; a single coalescence, red; and multiple coalescence, blue.

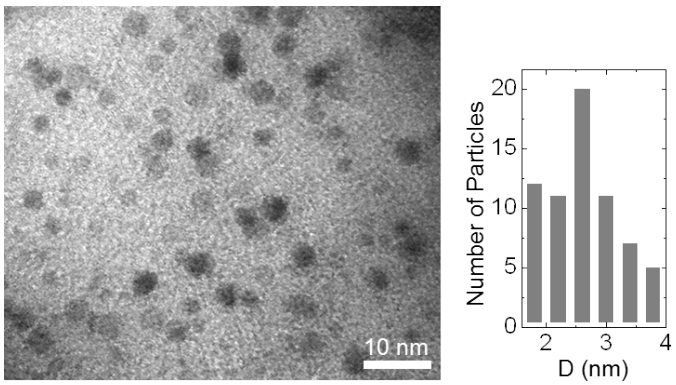

Figure A1.2. Bright-field TEM image of Pt NCs synthesized in a graphene liquid cell by the exposure of the growth solution to the electron beam for about 5 min and with corresponding particle diameter (D) histogram.

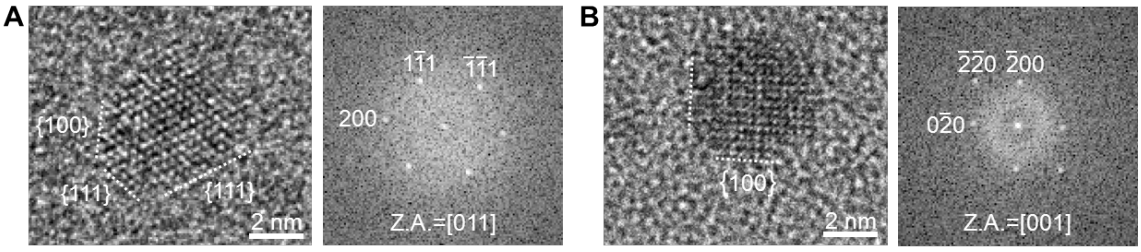

Figure A1.3. High-resolution TEM images and FFT patterns of Pt NCs **(A)** along the [011] zone axis (Z.A.) showing {100} and {111} facets and **(B)** along the [001] direction showing {100} facets.

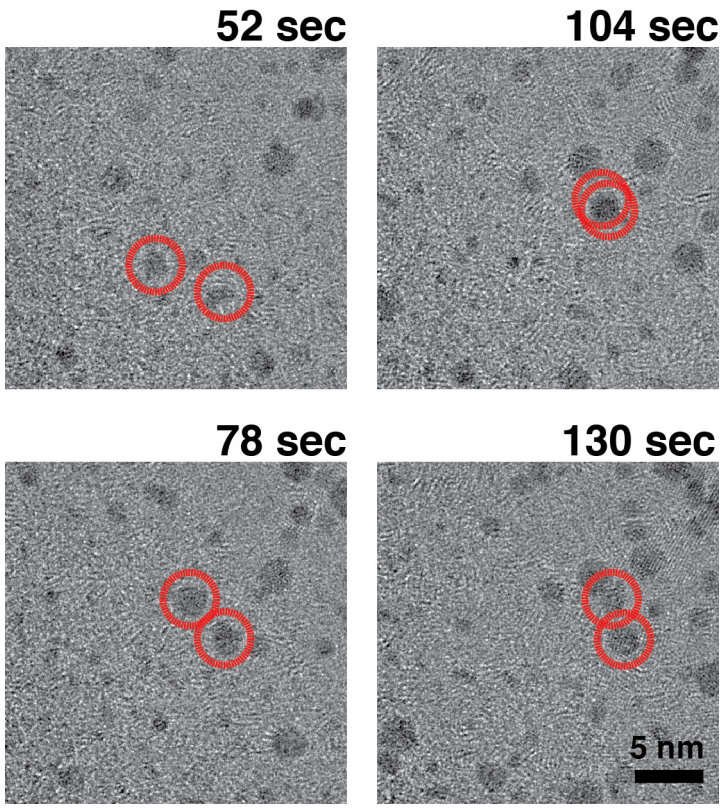

Figure A1.4. Stil snapshots of two NCs showing correlated motion before coalescence.

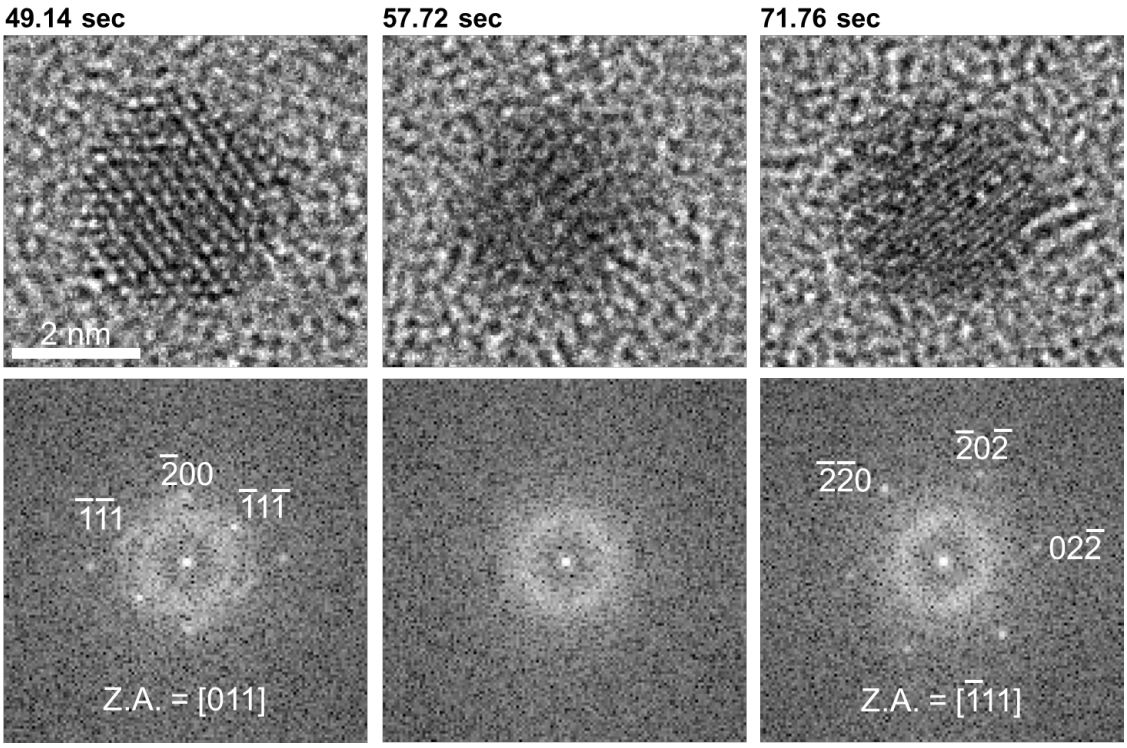

Figure A1.5. Still snapshots and fast Fourier transformed (FFT) patterns showing free rotation of a NC in GLC. The NC is on [011] zone axis at 49.14 sec, rotates off zone axis at 57.72 sec, and has [$\bar{1}$11] zone axis at 71.76 sec.

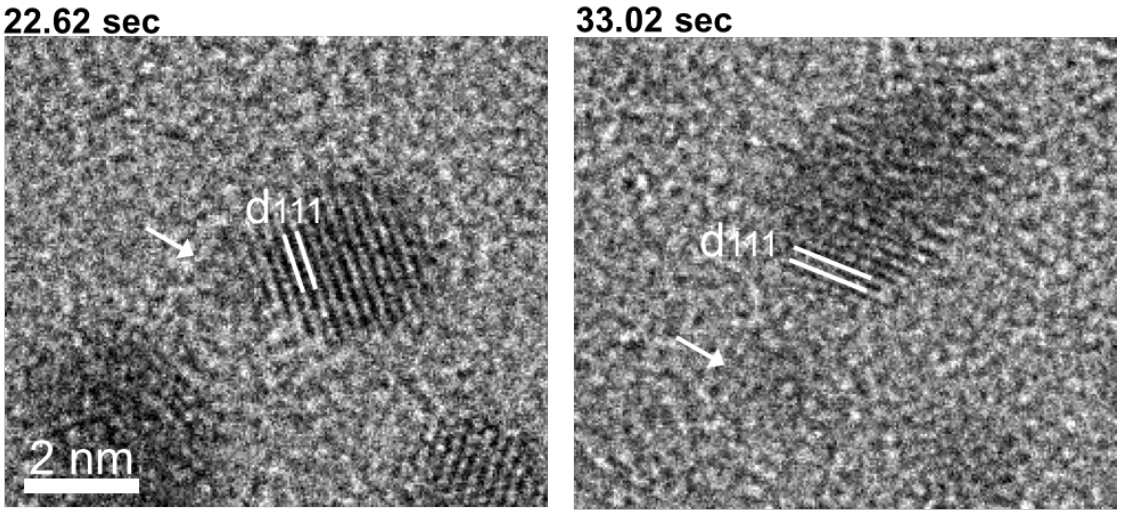

Figure A1.6. Still snapshots showing coalescence of Pt NCs on or near [011] zone axis. Coalescence evens happen at {111} planes in one of two NCs at 22.62 and 33.02 sec. Incoming small NCs indicated by arrows do not have any zone axes.

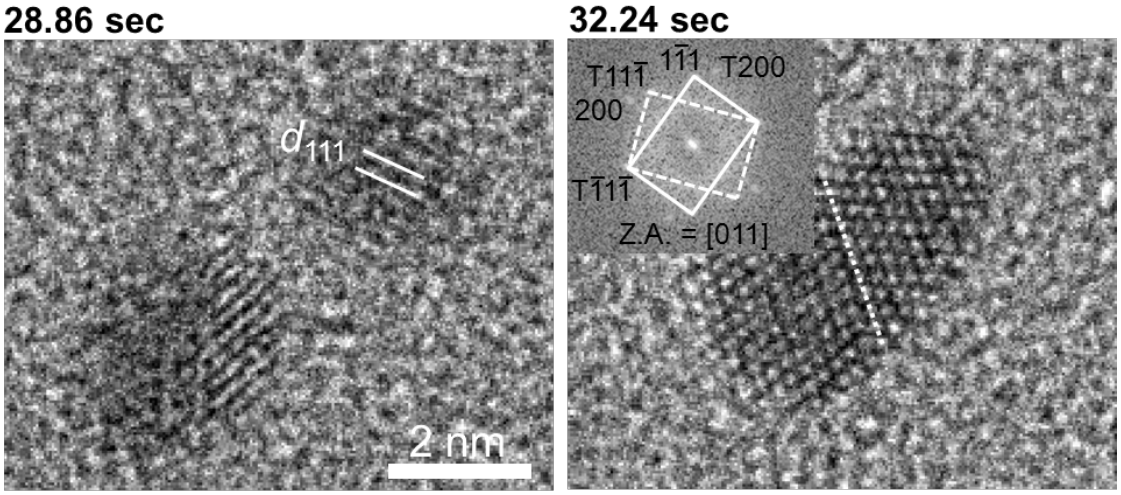

Figure A1.7. Still snapshots showing the twin boundary in a merged NC after coalescence of NCs on or near [011] zone axis. At 28.86 sec, the ratio of two NC diameters before coalescence is 0.88, which is similar with 0.86 of diameter ratio of two domains with twin boundary (dotted line) at 32.24 sec after coalescence.

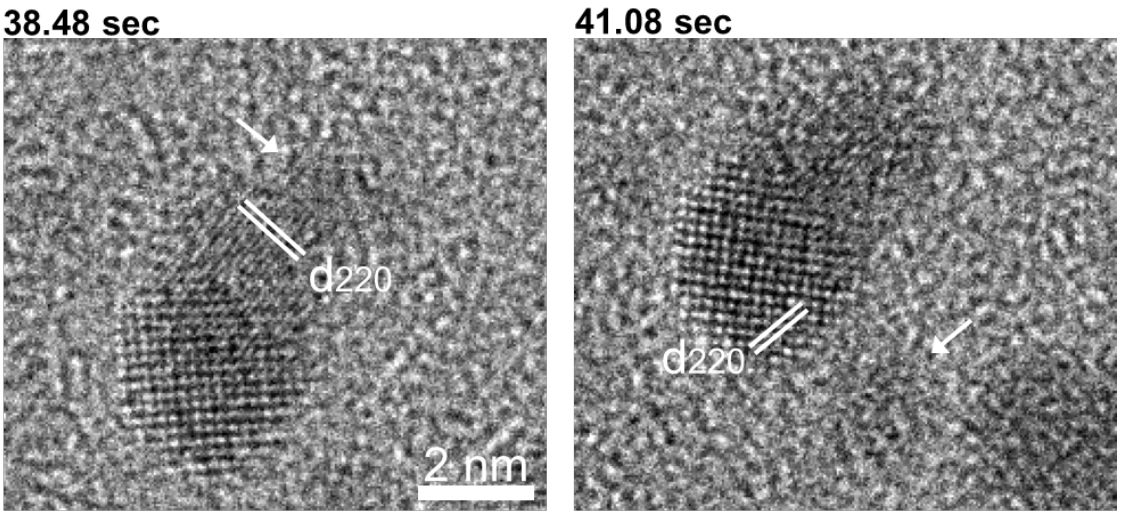

Figure A1.8. Still snapshots showing coalescence of Pt NCs on or near [001] zone axis. Coalescence evens happen at {110} planes in one of two NCs at 38.48 and 41.08 sec. Incoming small NCs indicated by arrows do not have any zone axes.

A2. Supporting Information for Direct Observation of Nanocrystal Superlattice Formation by Using Liquid Cell Transmission Electron Microscopy

A2.1. NCs tracking method

Recognizing and linking all NCs positions in every time step from TEM movie was not efficient by currently accessible particle tracking algorithms because NCs are overlapped each other while they form dense agglomerates and some NCs are dragged by solvent over the limit that can be detected by algorithm in a given time frame. In addition, non-zero background contrast compared to NCs due to the presence of solvent prohibits efficient detecting process. For image analysis shown in main manuscript, 51 NCs forming an assembled domain in the final stage were selected from final frame of Movie 1 and tracked in inverse time sequence. Two dimensional position of these selected NCs in different time frames were taken by combination of single-particle tracking method developed for live cell imaging and Image-J software package released by National Institutes of Health. After taking position of NCs with 1/3 sec time interval, center of 51 NCs and their relative positions for each time frame were calculated for the correction of thermal drift effect as follow:

$$(Cx, Cy) = \left(\frac{1}{N}\sum_{i=1}^{N} x_i \ , \frac{1}{N}\sum_{i=1}^{N} y_i \right);\ (Rx_i, Ry_i) = (\ x_i - Cx, y_i - Cy)$$

,where $(x_i, y_i), (Cx, Cy), and\ (Rx_i, Ry_i)$ are original position, center of NCs, and relative position, respectively for *N* number of NCs. Entire trajectories of 51 NCs obtained from this process are shown in Fig. S1.

A2.2. Additional figures

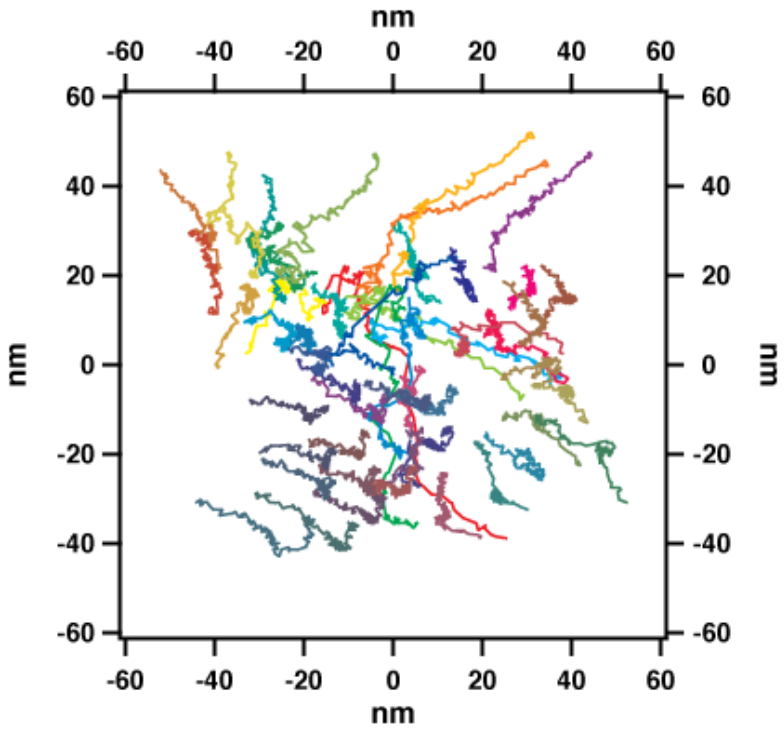

Figure A2.1. Trajectories of relative position of selected 51 NCs from.

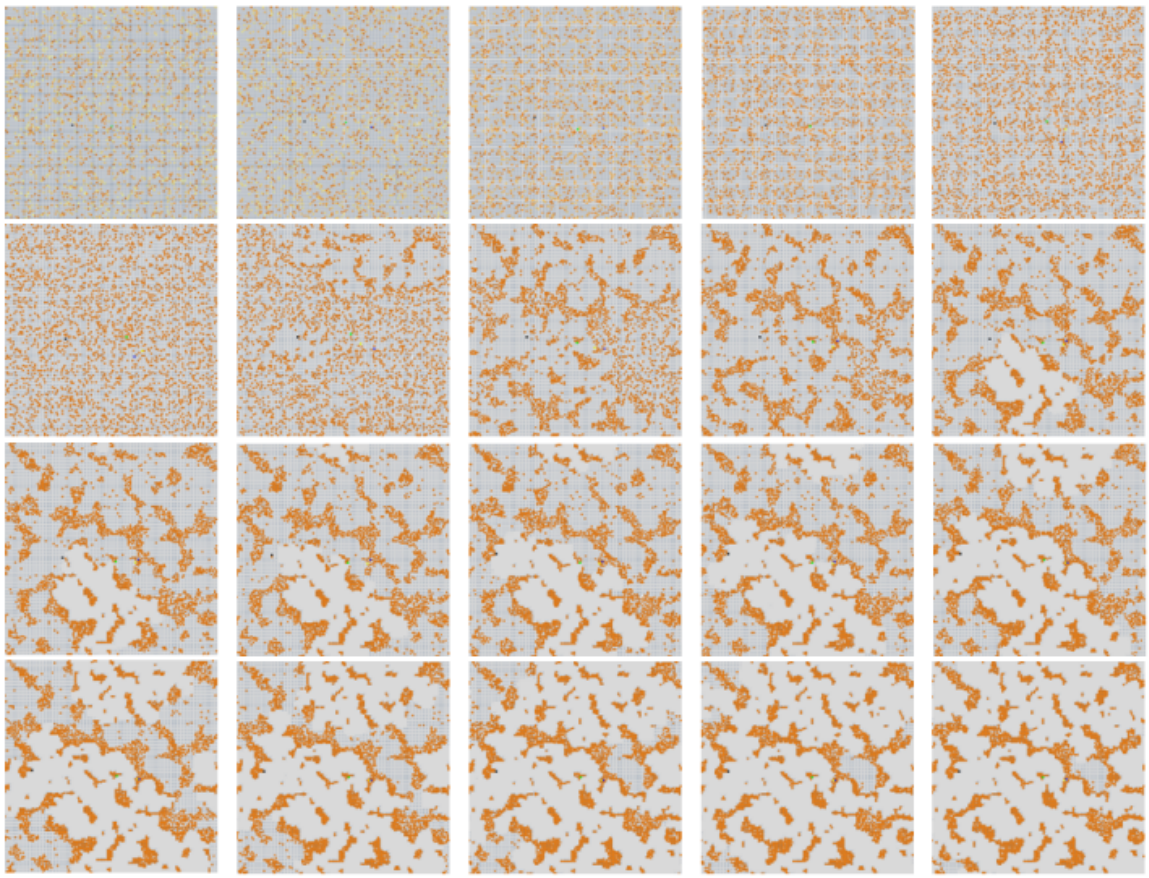

Figure A2.2. Simulated trajectory showing the full time range from an initial random phase to the assembled phase. Time frames for each image from top left to bottom right are 0, 1000, 2000, 3000, 4000, 10000, 15000, 20000, 22500, 25000, 25200, 25400, 25600, 25800, 26000, 26200, 26400, 26600, 26800, 27000 in MC units, respectively. Darker yellow color indicates NCs closer to substrate. Parameters are specified in the caption of Fig. 1.

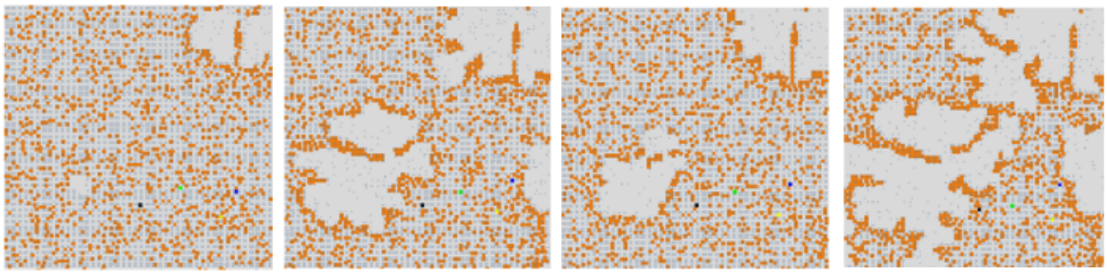

Figure A2.3. Simulated trajectories showing how NCs are dragged by the solvent front (upper right corner in each image). Time frame from left to right are 900, 1300, 1700, and 2100 in MC steps, respectively. Parameters are identical to those in Fig. 1 with $\mu = -3\frac{1}{4}\varepsilon_\ell$ and $T = 2\varepsilon_\ell$.

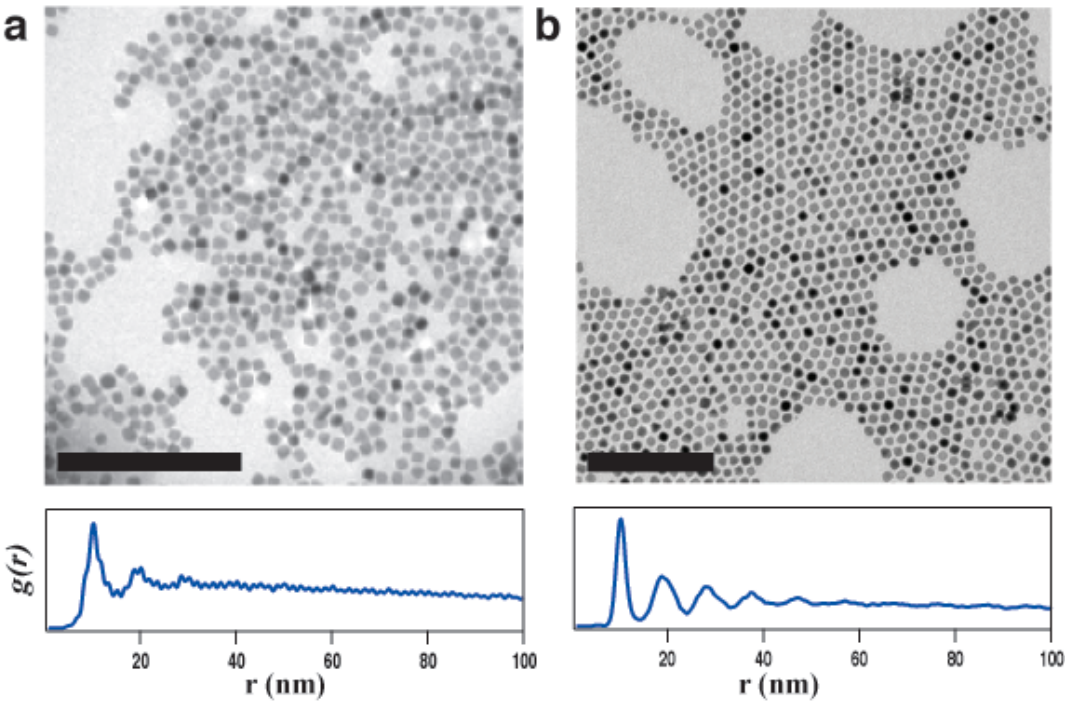

Figure A2.4. TEM images and radial-distribution functions of NCs assemblies formed under electron beam irradiation (panels (a)) and drop casting (panels (b))on SiNx TEM grid. The scale bar is 100 nm.

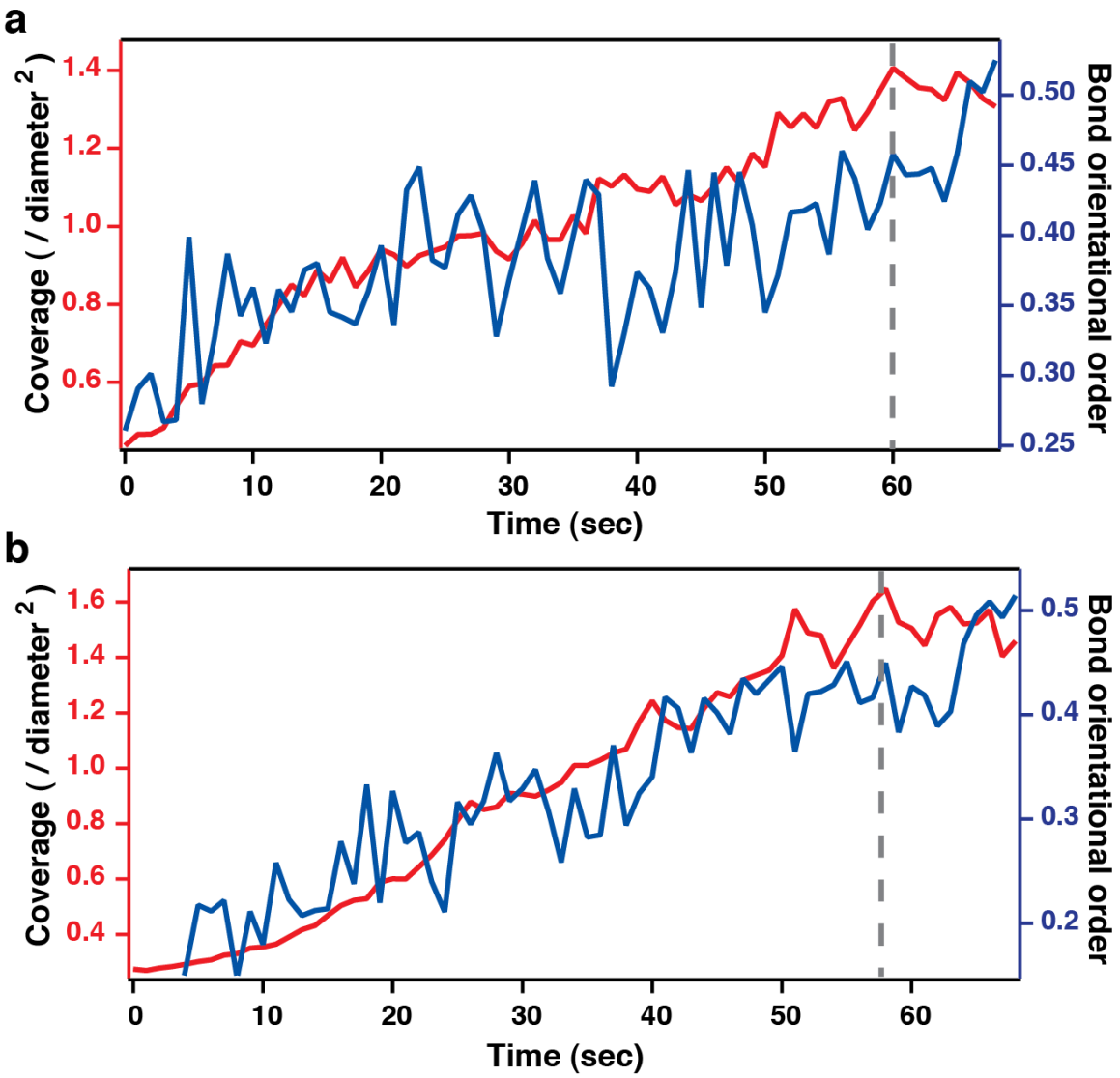

Figure A2.5. (a) and (b) Surface coverage of NCs and the 2D bond orientational order parameter, a measure of crystalline ordering, as a function of time. Two groups of NCs forming two separate domains in the final stage of self-assembly are tracked in (a) and (b).

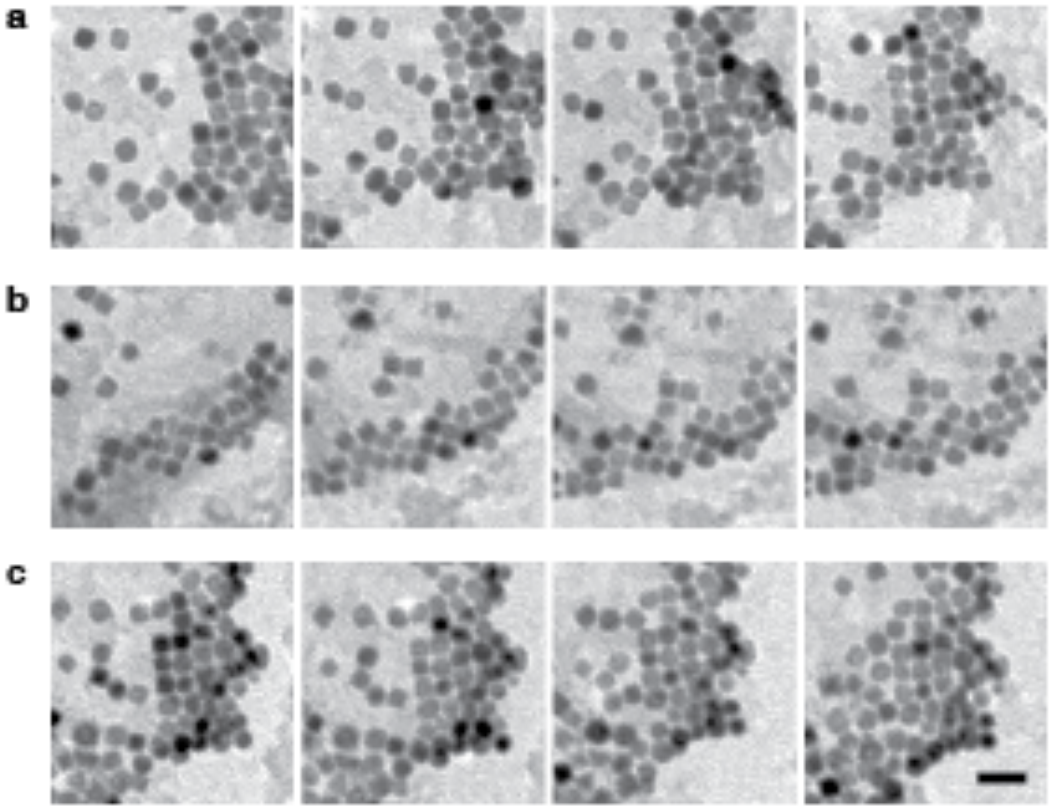

Figure A2.6. Domain growth by the addition of multiple NCs. (a) two NCs, (b) three NCs, and (c) four NCs add onto domain. The scale bar is 25 nm.

A3. Matlab script for Direct Observation of Nanocrystal Superlattice Formation by Using Liquid Cell Transmission Electron Microscopy

A3.1. Areal density and bond orientational order parameter.

```
% Load a file containing nanoparticle positions

clear all;
fid=fopen('Coord_selected_rev_51_unique.txt','r');
AA=fscanf(fid,'%f',[5, inf]);
fclose(fid);
BB=AA';


% Input parameters & load NP positions

d_critical = 14.26; % to consider particle-particle distances (<14.26nm)
d_particle=7.27;
N_frame=104;
N_particle=51;
C_distance_per_pixel=100./63.;
C_time_per_frame=1./3.;
x_max=(158-1)*C_distance_per_pixel;
y_max=(160-1)*C_distance_per_pixel;

frame_number=BB(1:N_frame,2);
time=(frame_number-1)*C_time_per_frame;

x_pixel_total=BB(:,3);
y_pixel_total=BB(:,4);
x_position_total=C_distance_per_pixel*(x_pixel_total-1);
y_position_total=C_distance_per_pixel*(160-y_pixel_total);


%Declare matrix for x and y positions of 51 NPs as time

positions=zeros(N_frame,2*N_particle);
x_positions=[];
y_positions=[];

for ii=1:N_particle
   positions(:,2*ii-1)=x_position_total((ii-1)*N_frame+1:ii*N_frame);
   positions(:,2*ii)=y_position_total((ii-1)*N_frame+1:ii*N_frame);
   x_positions=[x_positions positions(:,2*ii-1)];
```

```
    y_positions=[y_positions positions(:,2*ii)];
end

x_relative = x_positions - mean(x_positions,2)*ones(1,N_particle);
y_relative = y_positions - mean(y_positions,2)*ones(1,N_particle);



% Calculate local areal densities (or local coverd areas) and
% bond-orientational order parameters of each NP as a fct of time

psi6_j=zeros(N_frame,N_particle);
local_density=zeros(N_frame, N_particle);
local_covered_area =zeros(N_frame, N_particle);

for ii=1:N_frame
    tri = delaunay(x_relative(ii,:),y_relative(ii,:));
    NP_connection = zeros(N_particle);
    for jj=1:length(tri)
        NP_connection(tri(jj,1),tri(jj,2))=1;
        NP_connection(tri(jj,2),tri(jj,1))=1;
        NP_connection(tri(jj,2),tri(jj,3))=1;
        NP_connection(tri(jj,3),tri(jj,2))=1;
        NP_connection(tri(jj,3),tri(jj,1))=1;
        NP_connection(tri(jj,1),tri(jj,3))=1;
    end
    OnetoN=1:N_particle;
    psi_6=zeros(1,N_particle);

    for jj=1:N_particle
        connected_NPs=OnetoN(NP_connection(jj,:)>0);
        x_connected = x_relative(ii,connected_NPs);
        y_connected = y_relative(ii,connected_NPs);

        pp_distance = abs(x_connected-x_relative(ii,jj)+1i*(y_connected-y_relative(ii,jj)));

        x_neighbor = x_connected(pp_distance <d_critical);
        y_neighbor = y_connected(pp_distance <d_critical);

        if length(x_neighbor)<1.5
            psi_6(jj) = 0.;
            psi6_j(ii,jj) = 0.;
        else
            theta_jk = angle(x_connected-x_relative(ii,jj)+1i*(y_connected-y_relative(ii,jj)));
            psi_6(jj)=sum(exp(6i*theta_jk))/length(theta_jk);
            psi6_j(ii,jj)=sum(exp(6i*theta_jk))/length(theta_jk);
```

```
        end

        x_interval_c = x_relative(ii,jj);
        y_interval_c = y_relative(ii,jj);

        N_halfmesh = floor(d_critical/0.1);

        R_meshdist = N_halfmesh/d_critical;

        Total_area_local = ones(2*N_halfmesh+1,2*N_halfmesh+1)<0;

        for aa = 1:2*N_halfmesh+1
           for bb = 1:2*N_halfmesh+1
              x3 = (bb - N_halfmesh-1)/R_meshdist + x_relative(ii,jj);
              y3 = (N_halfmesh+1 - aa)/R_meshdist + y_relative(ii,jj);

              distance_check = ((x3-x_relative(ii,jj))^2+(y3-y_relative(ii,jj)).^2).^0.5 <
d_critical;
              distance_check2 = (y_relative(ii,jj)-y_connected).*(y3-y_relative(ii,jj)/2-
y_connected/2) < -(x_relative(ii,jj)-x_connected).*(x3-x_relative(ii,jj)/2-x_connected/2);
              Total_area_local(aa,bb)=distance_check & (sum(distance_check2)<0.5);
           end
        end

        local_covered_area(ii,jj)=sum(sum(Total_area_local))./R_meshdist^2;
        local_density(ii,jj)=pi*d_critical^2./ sum(sum(Total_area_local))*R_meshdist^2;
     end
end


% Classify nanoparticles with their local areal densities:
local_density_nor = local_density ./pi ./ d_critical^2 .* d_particle^2;
mean_local_density_nor = mean(local_density_nor);
g1= mean_local_density_nor >0.58;
g2= ~g1;

N_g1_particle=sum(g1);
x_g1_relative = x_relative(:,g1);
y_g1_relative = y_relative(:,g1);

N_g2_particle=sum(g2);
x_g2_relative = x_relative(:,g2);
y_g2_relative = y_relative(:,g2);


% Calculate areal densities and bond-orientational order parameters of two groups
```

```
total_covered_area = sum(local_covered_area,2);
total_density = N_particle * d_particle^2 ./ total_covered_area;
covered_area_g1 = local_covered_area * g1';
covered_area_g2 = local_covered_area * g2';
density_g1 = N_g1_particle * d_particle^2 ./ covered_area_g1;
density_g2 = N_g2_particle * d_particle^2 ./ covered_area_g2;

BOP1_total = sum(abs(psi6_j),2) ./ N_particle;
BOP1_g1=abs(psi6_j) * g1' ./ N_g1_particle;
BOP1_g2=abs(psi6_j) * g2' ./ N_g2_particle;


% Draw figures
figure;
plot(x_g1_relative(104,:), y_g1_relative(104,:), '.r', x_g2_relative(104,:),
y_g2_relative(104,:), '.b');

figure;
subplot(2,1,1), plot(time(:,1),total_density(:,1),'.-'); title('Total'); ylabel('Areal density');
subplot(2,1,2), plot(time(:,1),BOP1_total,'.-'); axis([0 70 0.25 0.55]); ylabel('psi_6');

figure;
subplot(2,1,1), plot(time(:,1),density_g1(:,1),'.-'); title('Group 1'); ylabel('Areal density');
subplot(2,1,2), plot(time(:,1),BOP1_g1,'.-'); axis([0 70 0.25 0.55]); ylabel('psi_6');

figure;
subplot(2,1,1), plot(time(:,1),density_g2(:,1),'.-'); title('Group 2'); ylabel('Areal density');
subplot(2,1,2), plot(time(:,1),BOP1_g2,'.-'); ylabel('psi_6');


% For exporting data to other programs

positions_g1 = [];
x_g1_relative_T = x_g1_relative';
y_g1_relative_T = y_g1_relative';
positions_g2 = [];
x_g2_relative_T = x_g2_relative';
y_g2_relative_T = y_g2_relative';

for ii=1:N_frame
   positions_g1 = [positions_g1 [time(ii) time(ii);x_g1_relative_T(:,ii)
y_g1_relative_T(:,ii)]];
   positions_g2 = [positions_g2 [time(ii) time(ii);x_g2_relative_T(:,ii)
y_g2_relative_T(:,ii)]];
end
```

A3.2. Delauney triangulation, density, and bond orientationla order parameter of high volume fraction nanoparticle solution.

```
% Input parameters

clear all;

C_distance_per_pixel=100./63.;
d_critical = 14.26; % to consider particle-particle distances (<14.26nm)
d_particle=7.27;

% Load three files containing NP positions of three different time frames

fid=fopen('Frame_100_position.txt','r');
AA1=fscanf(fid,'%f',[2, inf]);
fclose(fid);

N_particle_t1=length(AA1);
x_positions_t1=C_distance_per_pixel*AA1(1,:);
y_positions_t1=C_distance_per_pixel*(160-AA1(2,:));

fid=fopen('Frame_500_position.txt','r');
AA2=fscanf(fid,'%f',[2, inf]);
fclose(fid);

N_particle_t2=length(AA2);
x_positions_t2=C_distance_per_pixel*AA2(1,:);
y_positions_t2=C_distance_per_pixel*(160-AA2(2,:));

fid=fopen('Frame_1200_position.txt','r');
AA3=fscanf(fid,'%f',[2, inf]);
fclose(fid);

N_particle_t3=length(AA3);
x_positions_t3=C_distance_per_pixel*AA3(1,:);
y_positions_t3=C_distance_per_pixel*(160-AA3(2,:));


% Time 1: DeLaunay triangulation

x_positions = x_positions_t1;
y_positions = y_positions_t1;
N_particle = N_particle_t1;
```

```
tri_t1 = delaunay(x_positions,y_positions);
tri = tri_t1;

NP_connection = zeros(N_particle);
for jj=1:length(tri)
   NP_connection(tri(jj,1),tri(jj,2))=1;
   NP_connection(tri(jj,2),tri(jj,1))=1;
   NP_connection(tri(jj,2),tri(jj,3))=1;
   NP_connection(tri(jj,3),tri(jj,2))=1;
   NP_connection(tri(jj,3),tri(jj,1))=1;
   NP_connection(tri(jj,1),tri(jj,3))=1;
end


% Time 1: Calculate the areal density and bond-orientational order parameter

OnetoN=1:N_particle;
psi6_j=zeros(1,N_particle);
local_covered_area=zeros(1,N_particle);
local_density=zeros(1,N_particle);

for jj=1:N_particle
   connected_NPs=OnetoN(NP_connection(jj,:)>0);
   x_connected = x_positions(connected_NPs);
   y_connected = y_positions(connected_NPs);

   pp_distance = abs(x_connected-x_positions(jj)+1i*(y_connected-y_positions(jj)));

   x_neighbor = x_connected(pp_distance <d_critical);
   y_neighbor = y_connected(pp_distance <d_critical);

   if length(x_neighbor)<1.5
      psi6_j(jj) = 0.;
   else
      theta_jk = angle(x_connected-x_positions(jj)+1i*(y_connected-y_positions(jj)));
      psi6_j(jj)=sum(exp(6i*theta_jk))/length(theta_jk);
   end

   x_interval_c = x_positions(jj);
   y_interval_c = y_positions(jj);

   N_halfmesh = floor(d_critical/0.3);

   R_meshdist = N_halfmesh/d_critical;

   Total_area_local = ones(2*N_halfmesh+1,2*N_halfmesh+1)<0;
```

```
    for aa = 1:2*N_halfmesh+1
        for bb = 1:2*N_halfmesh+1
            x3 = (bb - N_halfmesh-1)/R_meshdist + x_positions(jj);
            y3 = (N_halfmesh+1 - aa)/R_meshdist + y_positions(jj);

            distance_check = ((x3-x_positions(jj))^2+(y3-y_positions(jj)).^2).^0.5 <
d_critical;
            distance_check2 = (y_positions(jj)-y_connected).*(y3-y_positions(jj)/2-
y_connected/2) < -(x_positions(jj)-x_connected).*(x3-x_positions(jj)/2-x_connected/2);
            Total_area_local(aa,bb)=distance_check & (sum(distance_check2)<0.5);
        end
    end

    local_covered_area(jj)=sum(sum(Total_area_local))./R_meshdist^2;
    local_density(jj)=pi*d_critical^2./ sum(sum(Total_area_local))*R_meshdist^2;

end

total_covered_area = sum(local_covered_area);
total_density_t1 = N_particle * d_particle^2 / total_covered_area;
BOP1_total_t1 = sum(abs(psi6_j)) / N_particle;


% Time 2: DeLaunay triangulation

positions_t2=[x_positions_t2;y_positions_t2];
positions_t2_u=(unique(positions_t2','rows'))';

x_positions_t2_u = positions_t2_u(1,:);
y_positions_t2_u = positions_t2_u(2,:);
N_particle_t2_u = length(positions_t2_u);

x_positions = x_positions_t2_u;
y_positions = y_positions_t2_u;
N_particle = N_particle_t2_u;


tri_t2 = delaunay(x_positions,y_positions);
tri = tri_t2;

NP_connection = zeros(N_particle);
for jj=1:length(tri)
    NP_connection(tri(jj,1),tri(jj,2))=1;
    NP_connection(tri(jj,2),tri(jj,1))=1;
    NP_connection(tri(jj,2),tri(jj,3))=1;
```

```
    NP_connection(tri(jj,3),tri(jj,2))=1;
    NP_connection(tri(jj,3),tri(jj,1))=1;
    NP_connection(tri(jj,1),tri(jj,3))=1;
end


% Time 2: Calculate the areal density and bond-orientational order parameter

OnetoN=1:N_particle;
psi6_j=zeros(1,N_particle);
local_covered_area=zeros(1,N_particle);
local_density=zeros(1,N_particle);

for jj=1:N_particle
    connected_NPs=OnetoN(NP_connection(jj,:)>0);
    x_connected = x_positions(connected_NPs);
    y_connected = y_positions(connected_NPs);

    pp_distance = abs(x_connected-x_positions(jj)+1i*(y_connected-y_positions(jj)));

    x_neighbor = x_connected(pp_distance <d_critical);
    y_neighbor = y_connected(pp_distance <d_critical);

    if length(x_neighbor)<1.5
        psi6_j(jj) = 0.;
    else
        theta_jk = angle(x_connected-x_positions(jj)+1i*(y_connected-y_positions(jj)));
        psi6_j(jj)=sum(exp(6i*theta_jk))/length(theta_jk);
    end

    x_interval_c = x_positions(jj);
    y_interval_c = y_positions(jj);

    N_halfmesh = floor(d_critical/0.3);

    R_meshdist = N_halfmesh/d_critical;

    Total_area_local = ones(2*N_halfmesh+1,2*N_halfmesh+1)<0;

    for aa = 1:2*N_halfmesh+1
        for bb = 1:2*N_halfmesh+1
            x3 = (bb - N_halfmesh-1)/R_meshdist + x_positions(jj);
            y3 = (N_halfmesh+1 - aa)/R_meshdist + y_positions(jj);

            distance_check = ((x3-x_positions(jj))^2+(y3-y_positions(jj)).^2).^0.5 <
d_critical;
```

```
        distance_check2 = (y_positions(jj)-y_connected).*(y3-y_positions(jj)/2-
y_connected/2) < -(x_positions(jj)-x_connected).*(x3-x_positions(jj)/2-x_connected/2);
        Total_area_local(aa,bb)=distance_check & (sum(distance_check2)<0.5);
      end
   end

   local_covered_area(jj)=sum(sum(Total_area_local))./R_meshdist^2;
   local_density(jj)=pi*d_critical^2./ sum(sum(Total_area_local))*R_meshdist^2;

end

total_covered_area = sum(local_covered_area);
total_density_t2 = N_particle * d_particle^2 / total_covered_area;
BOP1_total_t2 = sum(abs(psi6_j)) / N_particle;


% Time 3: DeLaunay triangulation

positions_t3=[x_positions_t3;y_positions_t3];
positions_t3_u=(unique(positions_t3','rows'))';

x_positions_t3_u = positions_t3_u(1,:);
y_positions_t3_u = positions_t3_u(2,:);
N_particle_t3_u = length(positions_t3_u);

x_positions = x_positions_t3_u;
y_positions = y_positions_t3_u;
N_particle = N_particle_t3_u;

tri_t3 = delaunay(x_positions,y_positions);
tri = tri_t3;

NP_connection = zeros(N_particle);
for jj=1:length(tri)
   NP_connection(tri(jj,1),tri(jj,2))=1;
   NP_connection(tri(jj,2),tri(jj,1))=1;
   NP_connection(tri(jj,2),tri(jj,3))=1;
   NP_connection(tri(jj,3),tri(jj,2))=1;
   NP_connection(tri(jj,3),tri(jj,1))=1;
   NP_connection(tri(jj,1),tri(jj,3))=1;
end


% Time 3: Calculate the areal density and bond-orientational order parameter

OnetoN=1:N_particle;
```

```
psi6_j=zeros(1,N_particle);
local_covered_area=zeros(1,N_particle);
local_density=zeros(1,N_particle);

for jj=1:N_particle
   connected_NPs=OnetoN(NP_connection(jj,:)>0);
   x_connected = x_positions(connected_NPs);
   y_connected = y_positions(connected_NPs);

   pp_distance = abs(x_connected-x_positions(jj)+1i*(y_connected-y_positions(jj)));

   x_neighbor = x_connected(pp_distance <d_critical);
   y_neighbor = y_connected(pp_distance <d_critical);

   if length(x_neighbor)<1.5
      psi6_j(jj) = 0.;
   else
      theta_jk = angle(x_connected-x_positions(jj)+1i*(y_connected-y_positions(jj)));
      psi6_j(jj)=sum(exp(6i*theta_jk))/length(theta_jk);
   end

   x_interval_c = x_positions(jj);
   y_interval_c = y_positions(jj);

   N_halfmesh = floor(d_critical/0.3);

   R_meshdist = N_halfmesh/d_critical;

   Total_area_local = ones(2*N_halfmesh+1,2*N_halfmesh+1)<0;

   for aa = 1:2*N_halfmesh+1
      for bb = 1:2*N_halfmesh+1
         x3 = (bb - N_halfmesh-1)/R_meshdist + x_positions(jj);
         y3 = (N_halfmesh+1 - aa)/R_meshdist + y_positions(jj);

         distance_check = ((x3-x_positions(jj))^2+(y3-y_positions(jj)).^2).^0.5 <
d_critical;
         distance_check2 = (y_positions(jj)-y_connected).*(y3-y_positions(jj)/2-
y_connected/2) < -(x_positions(jj)-x_connected).*(x3-x_positions(jj)/2-x_connected/2);
         Total_area_local(aa,bb)=distance_check & (sum(distance_check2)<0.5);
      end
   end

   local_covered_area(jj)=sum(sum(Total_area_local))./R_meshdist^2;
   local_density(jj)=pi*d_critical^2./ sum(sum(Total_area_local))*R_meshdist^2;
```

```
end

total_covered_area = sum(local_covered_area);
total_density_t3 = N_particle * d_particle^2 / total_covered_area;
BOP1_total_t3 = sum(abs(psi6_j)) / N_particle;

% Output cacluated data for three different time frames

N_particle_t1
total_density_t1
BOP1_total_t1
N_particle_t2_u
total_density_t2
BOP1_total_t2
N_particle_t3_u
total_density_t3
BOP1_total_t3

% Draw figures
figure; triplot(tri_t1,x_positions_t1,y_positions_t1); axis square; axis([100 275 50 225]);
figure; triplot(tri_t2,x_positions_t2_u,y_positions_t2_u); axis square; axis([100 275 50
225]);
figure; triplot(tri_t3,x_positions_t3_u,y_positions_t3_u); axis square; axis([100 275 50
225]);
```

A3.3. Radial distribution function.

```
% Input parameters
clear all;
fid=fopen('CellCounter_29000_000.txt','r');
AA=fscanf(fid,'%f',[5, inf]);
fclose(fid);
BB=AA';

N_particle=length(BB);
C_distance_per_pixel=100./544.;

x_pixel_total=BB(:,3);
y_pixel_total=BB(:,4);
x_position=C_distance_per_pixel*(x_pixel_total-1);
y_position=C_distance_per_pixel*(2048-y_pixel_total);

figure;
plot(x_position, y_position, '.');
x_position_s = x_position;
```

```
y_position_s = y_position;
N_particle_s = N_particle;
Area = 107919.82;

rr=(1:0.01:150)';
width_d=0.5;

% Plot radial distribution function
RDF=0*rr;
for jj=1:N_particle_s-1
   for kk=jj+1:N_particle_s
      rr0=((x_position_s(jj)-x_position_s(kk))^2 + (y_position_s(jj)-
y_position_s(kk))^2)^0.5;
      RDF = RDF + 1/width_d/pi^0.5/N_particle_s^2 / 2 * Area * exp(-(rr-
rr0).^2/width_d^2) ./ rr;
   end
end

figure;
plot(rr,RDF);
```